Cell Reports
Medicine

Article

Comprehensive single-cell metabolic profiling identifies targets to sensitize triple-negative breast cancer to chemo-immunotherapy

Graphical abstract

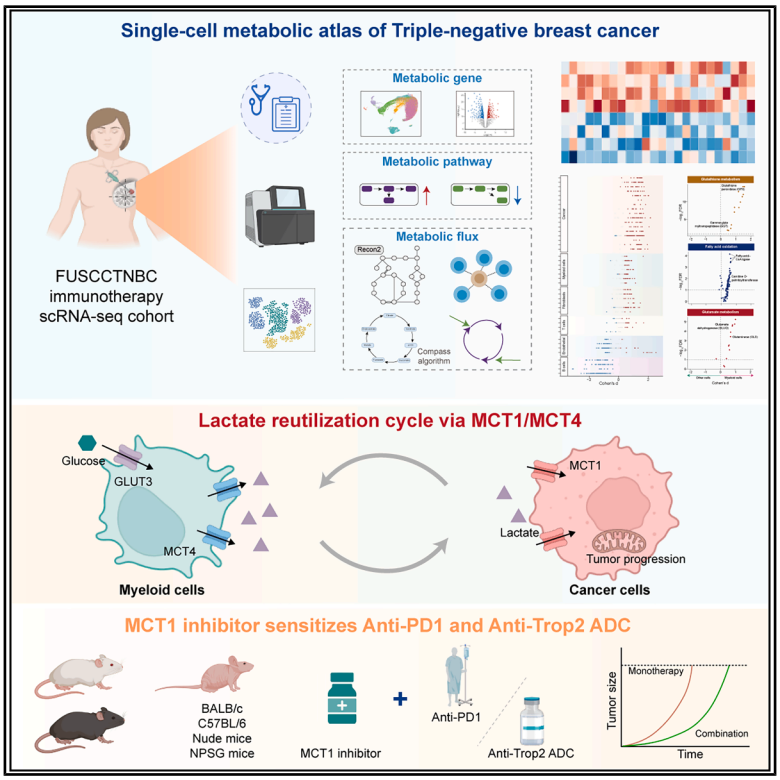

Highlights

- Single-cell profiling reveals metabolic heterogeneity across cell types in TNBC
- Cell-type-specific metabolic features improve prediction of therapy response
- Lactate reutilization axis between tumor and myeloid cells drives tumor progression
- MCT1 inhibition enhances antibody-drug conjugate and immunotherapy efficacy in TNBC

Authors

Ying Xu, Xin-Yi Liu, Hang Zhang, ..., Zhi-Ming Shao, Yi Xiao, Yi-Zhou Jiang

Correspondence

zhimingshao@fudan.edu.cn (Z.-M.S.), yixiao11@fudan.edu.cn (Y.X.), yizhoujiang@fudan.edu.cn (Y.-Z.J.)

In brief

Xu et al. perform comprehensive single-cell profiling to revealmetabolic heterogeneity of distinct cell types in the triple-negative breast cancer (TNBC) microenvironment and demonstrate the association between cell-type-specific metabolic traits with therapy response. MCT1/MCT4 axis mediates lactate reutilization to promote tumor progression and targeting this sensitizes immunotherapy and antibody-drug conjugate in TNBC.

Xu et al., 2026, Cell Reports Medicine 7, 102659
March 17, 2026
https://doi.org/10.1016/j.xcrm.2026.102659

CellPress

Cell Reports Medicine

CellPress
OPEN ACCESS

Article

Comprehensive single-cell metabolic profiling identifies targets to sensitize triple-negative breast cancer to chemo-immunotherapy

Ying Xu,[1,3] Xin-Yi Liu,[1,3] Hang Zhang,[1,3] Li Chen,[1,3] Han Wang,[1] Zhi-Ming Shao,[1,*] Yi Xiao,[1,*] and Yi-Zhou Jiang[1,2,4,*]
[1]Key Laboratory of Breast Cancer in Shanghai, Department of Breast Surgery, Fudan University Shanghai Cancer Center, Department of Oncology, Shanghai Medical College, Fudan University, Shanghai 200032, P.R. China
[2]Shanghai Academy of Natural Sciences (SANS), Fudan University, Shanghai 200032, P.R. China
[3]These authors contributed equally
[4]Lead contact
*Correspondence: zhimingshao@fudan.edu.cn (Z.-M.S.), yixiao11@fudan.edu.cn (Y.X.), yizhoujiang@fudan.edu.cn (Y.-Z.J.)
https://doi.org/10.1016/j.xcrm.2026.102659

SUMMARY

The treatment of triple-negative breast cancer (TNBC) poses significant challenges, necessitating innovative approaches to identify therapeutic targets. This study presents a cohort of patients with early-stage TNBC receiving neoadjuvant chemotherapy or chemo-immunotherapy, leveraging single-cell RNA sequencing and metabolic analysis to elucidate the impact of metabolic reprogramming on treatment response. Our findings reveal metabolic heterogeneity at levels of metabolic genes, pathways, and fluxes. Cell-type-specific metabolic traits show stronger associations with therapeutic response compared with bulk metabolic features and the proportion of major cell types. We identify a dynamic collaboration between tumor cells and myeloid cells driven by differential glucose utilization and lactate production, which facilitates tumor progression. Monocarboxylate transporter 1 (MCT1) inhibitors disrupt their interaction, enhancing the efficacy of anti-PD-1 and antibody-drug conjugate (ADC) treatments in TNBC mouse models. Overall, our study delineates the single-cell metabolic landscape of TNBC and positions MCT1 as a promising target.

INTRODUCTION

Triple-negative breast cancer (TNBC) is a highly aggressive disease and has the worst survival rate among all breast cancer subtypes.[1] Due to the absence of human epidermal growth factor receptor 2, progesterone receptor, and estrogen receptor, chemotherapy remains the primary treatment for TNBC.[2] Thankfully, the high specificity and affinity toward the antigen endow antibody-drug conjugates (ADCs) with improved therapeutic index, making them appealing treatment options for TNBC. Nonetheless, the treatment response of ADCs is ultimately limited by impaired lysosomal function and other mechanisms that confer drug resistance.[3] On the other hand, TNBC, which is characterized by higher immune cell infiltration in the tumor microenvironment (TME), is generally more responsive to immunotherapy than other breast cancer subtypes.[4] Several clinical trials have investigated chemo-immunotherapy combinations, showing promising prognostic improvements.[5–8] However, immune heterogeneity and escape mechanisms limit the response to immunotherapy, with only 3%–25% of TNBC patients benefiting.[9–11] Therefore, there exists a pressing unmet need to develop more effective combination therapeutic strategies to expand the population that effectively responds to ADC therapy and immunotherapy in TNBC.

As of now, an understanding of how TME metabolism orchestrates resistance to both cytotoxic and immune-based therapies in TNBC remains limited. Encouragingly, the advent of high-resolution technologies and innovative metabolic flux analysis methods has opened up remarkable opportunities for deciphering the intricate metabolic interactions within the TNBC ecosystem. Leveraging cutting-edge technologies such as single-cell RNA sequencing (scRNA-seq), researchers can now elucidate the metabolic characteristics of individual cells with unprecedented resolution and detail. Of particular significance are the flux balance analysis (FBA) methods, which enable precise *in silico* predictions of metabolic changes across the constructed metabolic database network.[12–14] For example, COMPASS could successfully predict metabolic targets across both central and ancillary pathways. The algorithm identifies Th17-pathogenicity-related pathways and functional key factors, including polyamines, independently validated by metabolomics data.[15] By harnessing the full potential of these advanced technologies and methodologies, researchers are now equipped to uncover the complex metabolic crosstalk and thoroughly delve into the realm of precision immune-metabolic therapy.[16]

In this study, we leveraged scRNA-seq data from our established discovery cohort to systematically explore the single-cell metabolic landscape of TNBC across three key dimensions: metabolic genes, metabolic pathways, and metabolic fluxes. We identified substantial metabolic heterogeneity across distinct cell types, with certain metabolic pathway activities correlating

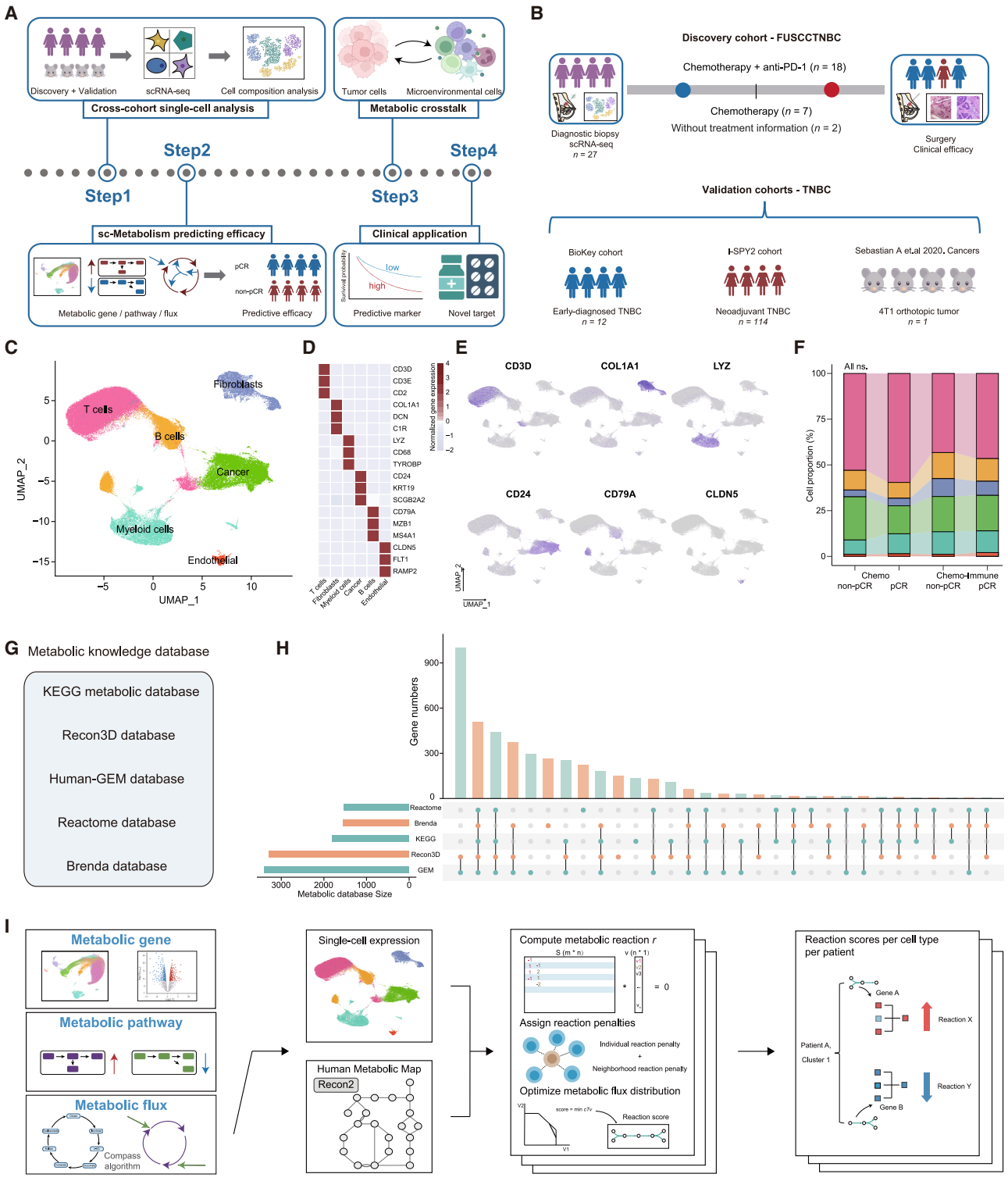

Figure 1. Schematic diagram of the cohort and metabolic analytical workflow

(A) Schematic overview of the analytical workflow performed in this study, showing patient cohorts and treatment arms.

(B) Overview of the discovery cohort and validation cohorts used in this study. The discovery cohort (FUSCCTNBC) consisted of 27 TNBC patients, including 18 treated with combined chemotherapy and anti-PD-1 immunotherapy and 7 with chemotherapy alone. The other 2 patients lacked treatment information, as described. Single-cell RNA sequencing (scRNA-seq) was performed on diagnostic biopsy samples before treatment, and clinical response was assessed at surgery. The validation cohorts (bottom) were analyzed to verify metabolic signatures and evaluate its prediction response.

(legend continued on next page)

with immunotherapy and chemotherapy response. Specifically, we found that differences in glucose and lactate utilization preferences between tumor cells and myeloid cells significantly contribute to TNBC progression. In addition to differential wiring of glucose metabolism, our work also identified monocarboxylate transporter 1 (MCT1) as a potential metabolic target of TNBC, which enhanced the efficacy of anti-PD-1 or sacituzumab govitecan (SG) treatments. Collectively, our study presented a comprehensive single-cell metabolic landscape and provided a feasible immune-metabolic treatment strategy for TNBC.

RESULTS

Study cohorts and metabolic analysis scheme

To elucidate the metabolic characteristics of individual cell types within the TNBC ecosystem and reveal the effect of their metabolic interplay on immunotherapy and chemotherapy response, we established a discovery scRNA-seq cohort comprising 27 patients diagnosed with early-stage TNBC (Figure 1A). Among them, 18 individuals were administered a combination of chemotherapy and anti-PD-1 as neoadjuvant therapy, while 7 patients were given chemotherapy alone. Two additional patients were also included in the metabolic analysis, one of whom was lost to follow-up and the other lacked available treatment information (Table S1). We also utilized various published TNBC scRNA-seq cohorts for external validation (Figure 1B).[17–21] After the implementation of stringent quality control, a total of 196,294 cells in our cohort with average 1,799 genes per cell were retained for subsequent analysis in our discovery cohort (Figure S1A). As previously reported in breast cancer and other malignancies, a clear separation was observed among all major cell types, including malignant epithelial cells, immune cells, fibroblasts, and endothelial cells (Figures 1C–1E). There were no significant differences in cell-type proportions between the pathological complete response (pCR) and non-pCR groups in either the chemotherapy or chemo-immunotherapy cohorts, warranting further deciphering of the characteristics (Figures 1F, S1B, and S1C).

To comprehensively analyze metabolic features, we integrated multiple metabolic gene sets and pathway databases to construct a unified knowledge base (Figures 1G and 1H; Table S2). The comprehensive metabolic analysis was pursued on three fronts: metabolic genes, metabolic pathways, and metabolic flux balance analysis (FBA). In terms of the FBA at the single-cell level, we employed the COMPASS algorithm to demonstrate the activities of the complex metabolic networks (Figure 1I).[15]

Altogether, we built the TNBC immunotherapy scRNA-seq cohort and refined the comprehensive metabolic analytical workflow to further decipher the metabolic heterogeneity and scrutinize the metabolic interplay.

Metabolic heterogeneity and activity of different cell types within TNBC microenvironment

As previously reported, we described the metabolic preferences of distinct cell types in TNBC microenvironment from the dimensions of metabolic genes, metabolic pathways, and metabolic fluxes. Taking an overall perspective, cell types were clearly separated in the t-distributed stochastic neighbor embedding (t-SNE) and uniform manifold approximation and projection (UMAP) plots of metabolic genes, pathways, and fluxes, suggesting the unique metabolic dysregulation patterns in specific cell types (Figures 2A and 2B).[22,23]

Then, we systematically evaluated the metabolic activity of each cell type to relatively determine the significance of their respective metabolic processes. At the gene level, we calculated the mean expression of metabolic genes, finding that tumor cells had the highest levels, while B cells exhibited the lowest (Figure 2C). Moving to the pathway level, we gained insights into how various metabolic pathways interact and the overall metabolic landscape within cells. Tumor cells exhibited the highest activities, followed by cancer-associated fibroblasts (CAFs), myeloid cells, and endothelial cells (Figure 2D). Given that metabolic pathways *in vivo* are interconnected and constantly in flux, metabolic flux analysis aims to exhibit metabolic fluxes and characterize cellular metabolic states. We leveraged Compass, an algorithm for comprehensive characterization of single-cell metabolism that displays fairly better applicability and robustness to evaluate the Compass reaction scores of each cell type in TNBC microenvironment. Tumor cells displayed the highest overall metabolic activity, consistent with their proliferative and biosynthetic demands. Notably, consistent with results from the dimensions of metabolic genes and pathways, myeloid cells and CAFs also display elevated metabolic activities at the level of metabolic fluxes, warranting further investigation (Figure 2E).

Our analysis exhibited the variability in metabolic processes and states among different cell types, that is, the metabolic heterogeneity. Considering that metabolic heterogeneity is crucial for understanding how different cell types adapt to changing conditions and maintain homeostasis, a more comprehensive characterization of the metabolic landscape within the TNBC microenvironment is urgently needed.

(C) Uniform manifold approximation and projection (UMAP) map of 196,294 cells, color-coded by annotated cell type, including cancer cells, fibroblasts, endothelial cells, myeloid cells, T cells, and B cells.
(D and E) Heatmap (D) and UMAP plots (E) depicting the expression of marker genes for each cell type.
(F) Stacked bar plots depicting proportions of each cell type in different treatment and response groups (chemo non-pCR, chemo pCR, chemo-immune non-pCR, and chemo-immune pCR).
(G) Overview of the construction of a comprehensive metabolic knowledge base by integrating multiple public databases, including KEGG, Recon3D, HumanGEM, Reactome, and Brenda.
(H) Detailed information about the integrated metabolic gene list across databases. The bar and UpSet plots showed overlapping and unique gene sets contributed by each database.
(I) Detailed metabolic analytical workflow, especially the metabolic flux algorithm, Compass. Compass leverages the topology and stoichiometry of the metabolic network to analyze single-cell RNA expression. Through this algorithm, we integrated scRNA-seq profiles with prior knowledge of the metabolic network to infer metabolic states of cells.

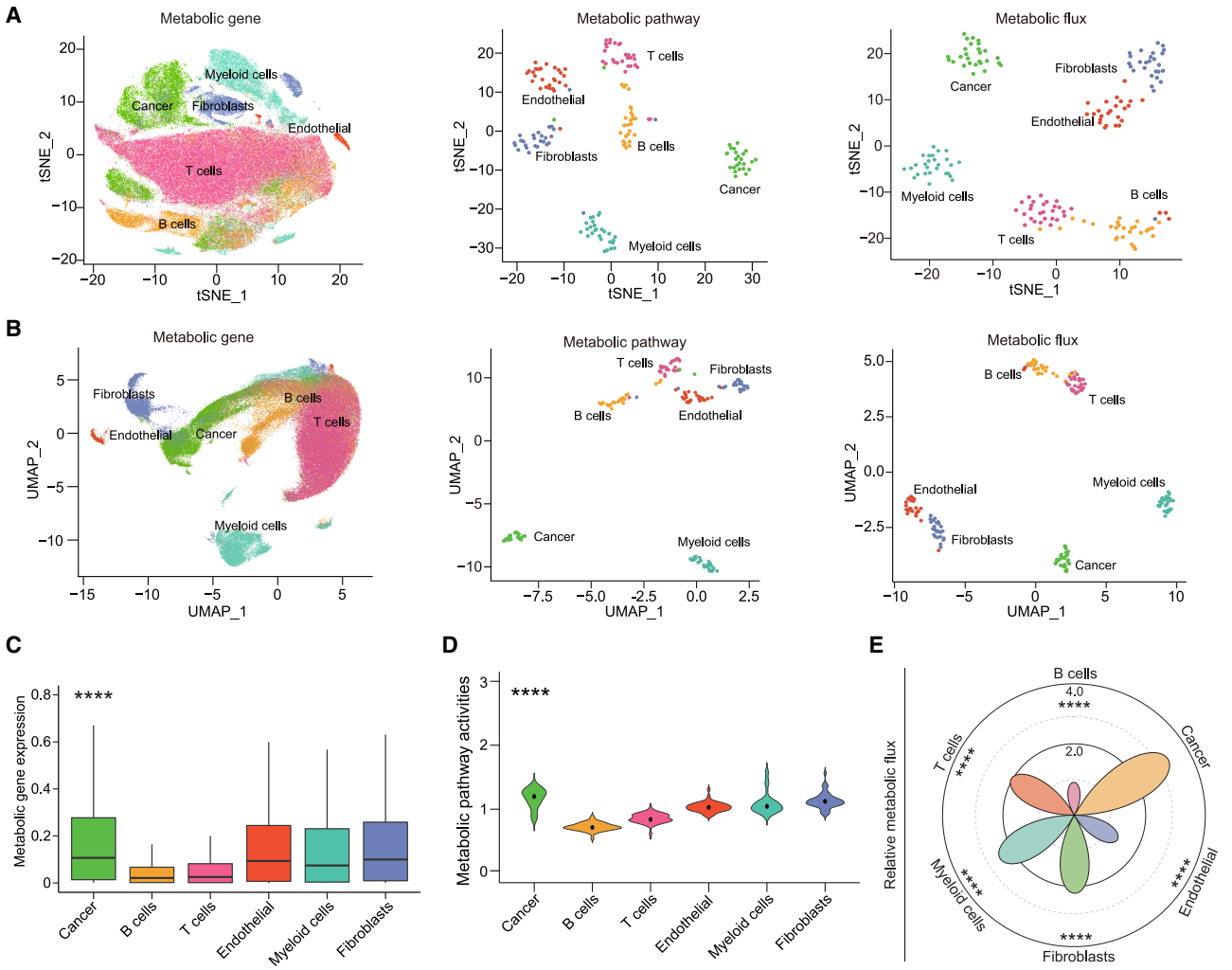

Figure 2. Metabolic heterogeneity of distinct cell types in the tumor microenvironment of TNBC

(A and B) T-distributed stochastic neighbor embedding (t-SNE, A) and uniform manifold approximation and projection (UMAP, B) plots of metabolic genes (left), pathways (middle), and fluxes (right), colored by cell types.

(C) The mean metabolic gene expression in different cell types for each patient were compared using the ANOVA.

(D) The metabolic pathway activities in different cell types for each patient were calculated by GSEA algorithm and compared using the ANOVA.

(E) Rose plot showing the relative metabolic flux across different cell types. Paired comparisons were performed between tumor cells and other cell populations using a paired *t* test. ****$p < 0.0001$; ***$p < 0.001$; **$p < 0.01$; *$p < 0.05$; ns, $p \geq 0.05$.

Distinct metabolic features of cell types in the microenvironment of TNBC

Then, we systematically characterized the detailed metabolic features of distinct cell types within the TNBC microenvironment (Figures 3A–3C; Tables S3–S5). To meet the demand for vigorous proliferation and mitigate the oxidative damage, tumor cells exhibited increased nutrient metabolism and elevated reliance on protective mechanisms against oxidative stress, as evidenced by the high expression of microsomal glutathione transferase 1 (MGST1) and glutathione s-transferase pi 1 (GSTP1) (Figures 3A and S1D). Aligning with metabolic gene levels, tumor cells exhibited significantly elevated metabolism in glycolysis/gluconeogenesis and glutathione-associated metabolism at pathway and flux levels (Figures 3B–3D and S2A). In terms of myeloid cells, we observed significant up-regulation of genes (such as apolipoprotein E [APOE] and apolipoprotein C1 [APOC1]), pathways, and fluxes related to lipid metabolism and peroxidation (Figure 3A). In addition, myeloid cells showed stronger activity in ferroptosis-associated pathways, including fatty acid oxidation, glutamate metabolism, and unsaturated fatty acid biosynthesis, suggesting a potential correlation between myeloid cells and ferroptosis (Figures 3B, 3E, S1E, and S2B). Increased proline and lysine metabolism and specific expression of nicotinamide N-methyltransferase (NNMT) in CAFs contributed to extracellular matrix remodeling, supporting cancer cell progression, and validating the rationale of our analysis (Figures S1F and S2C). As for one of the most crucial components of the anti-tumor immunity, T cells

CellPress
OPEN ACCESS

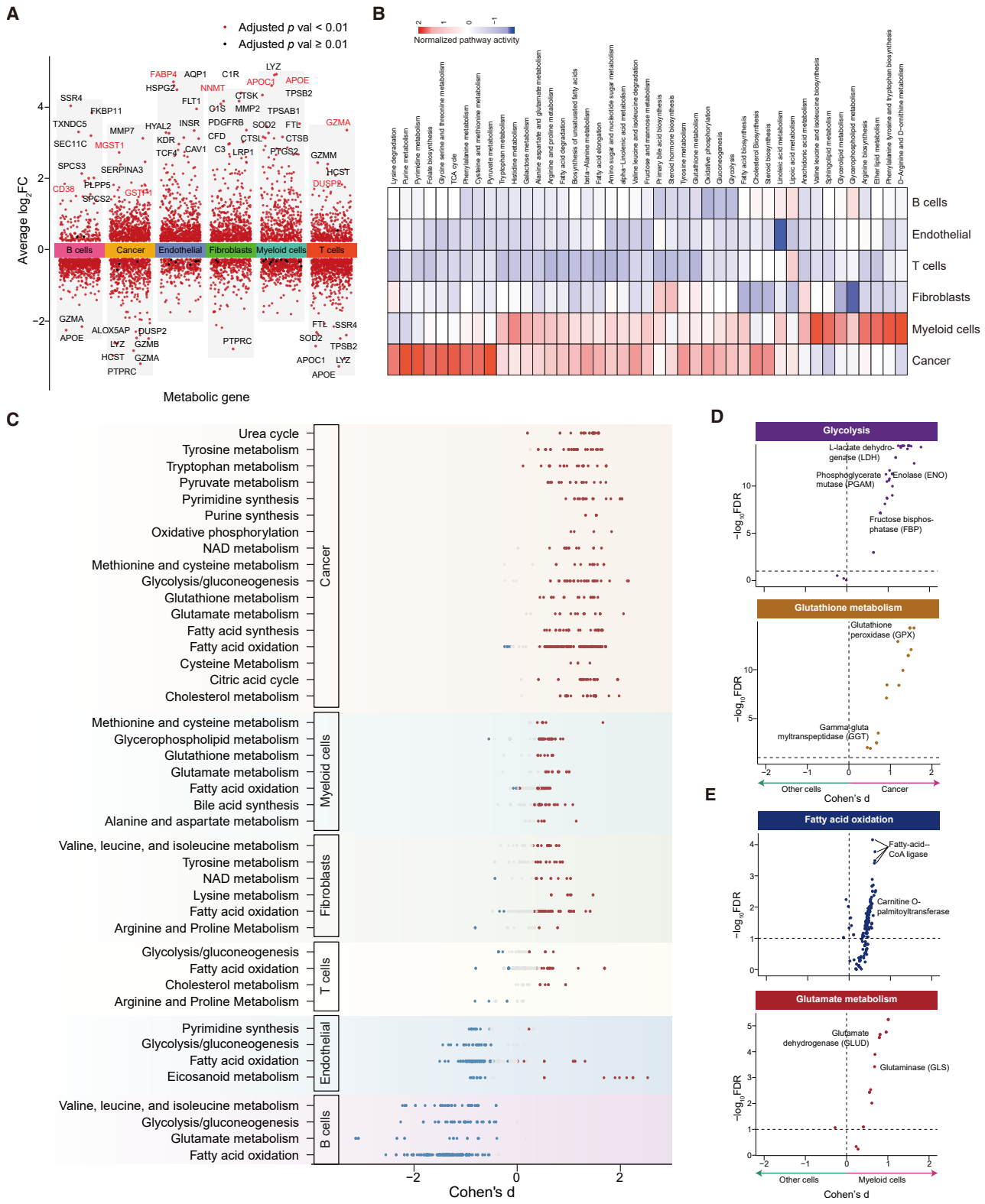

Figure 3. Distinct metabolic features of cell types in the tumor microenvironment of TNBC

(A) Differentially expressed metabolic genes across all cell types. Each cell type was compared with all remaining cells, and genes with adjusted p value < 0.01 is indicated in red, while an adjusted p value ≥ 0.01 is indicated in black.

(legend continued on next page)

exhibited the high expression of dual specificity phosphatase 2 (DUSP2) and granzyme A (GZMA) to regulate the immune cell function and inflammatory responses (Figure S1G). From the aspects of flux, T cells exhibited moderately elevated metabolism in fatty acid oxidation, indicating the role of lipid reprogramming in the anti-tumor process (Figure S2D). Interestingly, B cells appeared to exhibit high expression of a few metabolic genes like CD38 and relatively low metabolic flux activity in fatty acid metabolism, amino acid metabolism, and carbon metabolism (Figures S1H and S2E). Endothelial cells also showed increased expression of genes such as FABP4 and increased fluxes associated with lipid metabolism (Figures S1I and S2F). All crucial multidimensional metabolic characteristics are summarized in Table S6. The key results of our analysis were also externally validated in the BioKey cohort and the mouse TNBC scRNA-seq dataset, which supported the reliability of our analysis and provided a strong basis for further experiments (Figure S3).

In summary, we comprehensively described the metabolic landscape in TNBC at the single-cell level. Some of the key metabolic characteristics, especially those of cancer cells, myeloid cells, and CAFs, warrant further investigation for their role in metabolic interplay and tumor progression.

The integration of metabolic features in microenvironmental cells enhances the prediction of treatment response

Given that differences in cell-type proportions alone did not suffice to predict treatment response, we embarked on exploring whether the integration of cell-type proportions with metabolic features could enhance the prediction of chemotherapy or immunotherapy response (Figures 1F and S1C). Since the metabolic genes, pathways, and fluxes exhibit different points of focus on metabolic traits, as mentioned above, we assessed the overall metabolic differences in patients with different treatment response from these three perspectives. Although mean metabolic pathway scores and average metabolic gene expression were sometimes not statistically different between the pCR and non-pCR groups, relative mean metabolic flux activities of different cell types were significantly different (Figures S4A–S4C). Our findings suggested that metabolic activities of cell types might play an important role in predicting the treatment response of chemotherapy and immunotherapy.

Subsequently, we assessed the predictive potential of crucial metabolic pathways and genes in detail. From the perspective of metabolic pathways, we observed a significant positive correlation between most crucial metabolic pathway activities in the immune cells and pCR after chemotherapy and chemo-immunotherapy. In contrast, more active pathway activities of nucleotide, amino acid, and carbohydrate metabolism in CAFs indicated poor response after treatments. In addition, the predictive efficacy of pathway activities is heterogeneous in tumor cells, especially in terms of amino acid metabolism. While higher pathway activity levels for arginine biosynthesis and D-glutamine and D-glutamate metabolism were associated with better response in tumor cells, more active pathway activities of tyrosine metabolism and glutathione metabolism predicted non-pCR outcomes of chemo-immunotherapy (Figure 4).

Furthermore, similar results were obtained at the metabolic gene level (Figure S4D). For example, the upregulation of purine metabolism-related genes in CAFs like adenine phosphoribosyl transferase (APRT) indicated poor response after chemo-immunotherapy. Higher expression of fructose-1,6-bisphosphatase 1 (FBP1) in T cells, the key enzyme in glycolysis pathway, correlated with pCR outcomes of chemo-immunotherapy. Previous investigations have established the association between treatment response and lipid, amino acid, and carbohydrate metabolism in the context of chemotherapy or other targeted therapy, which validated the rationale and significance of our findings.[24–30] In contrast, cell-type proportions failed to demonstrate such predictive capabilities. We further assessed the predictive value of metabolic pathway scores and gene expression using bulk RNA-seq data from the I-SPY2 trial, which capture the overall activity of pathways or expression (Figure 4). However, only a limited number of pathways or genes demonstrated predictive potential. Notably, the steroid biosynthesis pathway showed concordant predictive performance with cell-type-specific analyses, whereas glutathione metabolism exhibited an opposite trend compared with predictions derived from specific cellular subpopulations. Thus, leveraging cell-type-specific metabolic activity has proven to be a more effective strategy for predicting treatment response, surpassing the predictive value of cell-type proportions or bulk-sequencing-based metabolic features. Mostly, focusing on key metabolic characteristics at the single-cell level and uncovering the underlying mechanisms, we could potentially refine and optimize current precision treatment strategies.

Distinct patterns of glucose utilization and lactate production in different microenvironment cell types

Given the high proportion of cancer cells and myeloid cells and the critical role of carbohydrate metabolism in TNBC, we further investigated the differences in the crucial energy metabolic pathway—central carbon metabolism—between these two cell types and the underlying mechanism.

First, we analyzed the variability in carbohydrate metabolism from the dimensions of metabolic genes and fluxes. We observed elevated expression of phosphofructokinase platelet (PFKP), lactate dehydrogenase B (LDHB), and oxoglutarate dehydrogenase L (OGDHL), as well as enhanced flux scores of glycolysis and TCA cycle in tumor cells. However, tumor cells showed lower expression of monocarboxylate transporter 4 (MCT4, also known as SLC16A3), as well as decreased flux scores of lactate secretion (Figures 5A–5C).

(B) Heatmap showing the normalized metabolic pathway enrichment scores of each cell type.
(C) Differential activity of metabolic reactions between the indicated cell type and other types. Reactions (dots) are partitioned by Recon2 pathways and colored by the sign of their Cohen's d statistic.
(D and E) Compass-score-based differential activity test of representative metabolic systems between cancer cells and other cells (D), as well as between myeloid cells and other cells (E).

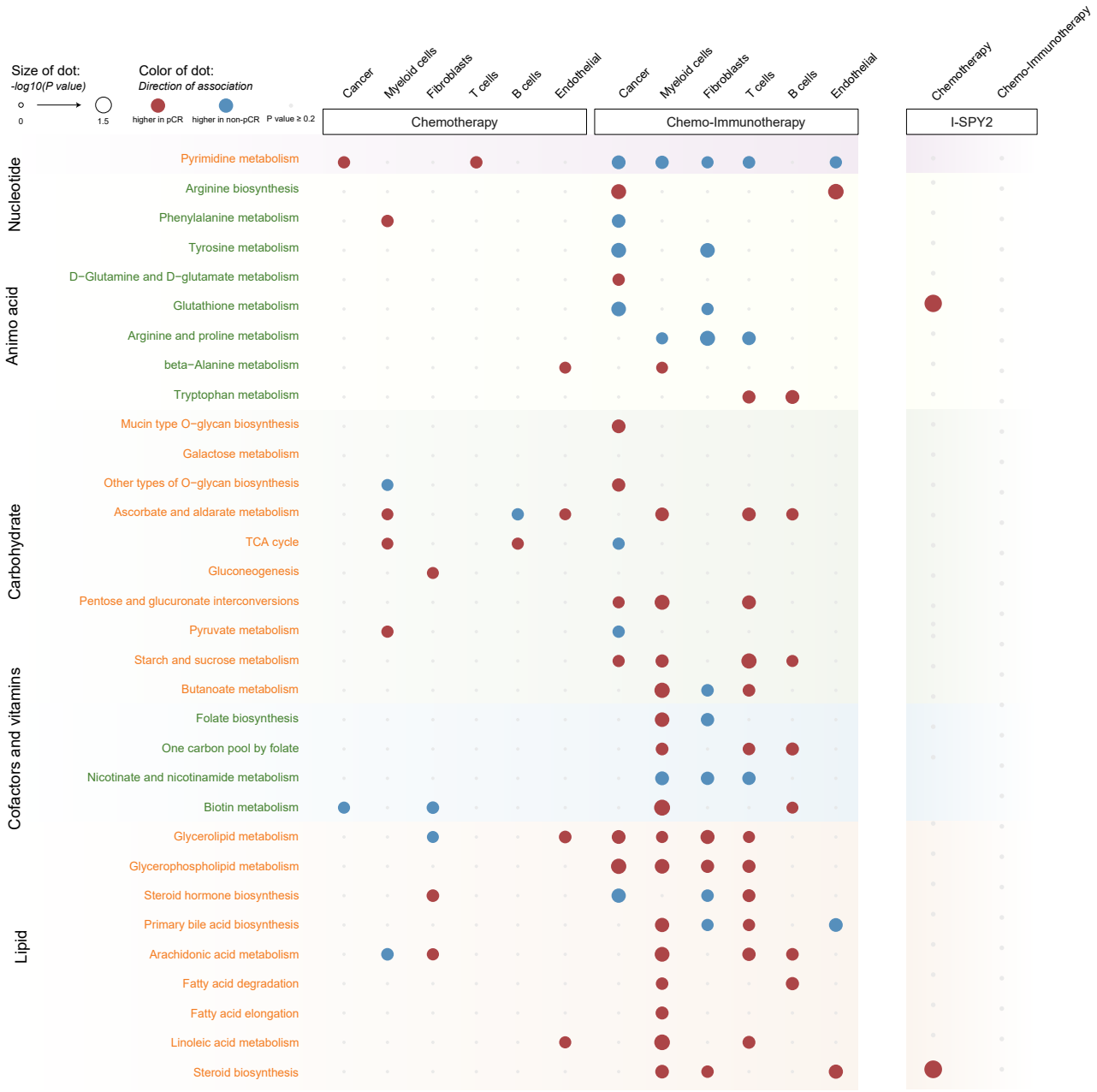

Figure 4. Metabolic features of microenvironmental cells are associated with therapeutic response to chemo-immunotherapy and chemotherapy

Dot plot showing the association between metabolic pathway activities and pCR. Metabolic pathway scores in different cell types for each patient were calculated by AUCell package, and averaged across all cells of the same type for each patient. Row labels denote metabolic pathway categories. Red/blue dots indicate higher/lower levels associated with pCR, whereas gray dots indicate $p \geq 0.2$; the size of dots reflects the p value. P values and associations were derived from logistic regression models.

These discoveries suggested that in addition to glucose-derived carbon in TCA cycle, tumor cells might have high demand to leverage readymade lactate as carbon source for carbohydrate metabolism to meet their high energy demands for rapid growth and proliferation. On the contrary, myeloid cells upregulated glucose transporter 3 (GLUT3, also known as SLC2A3) and MCT4 and exhibited higher fluxes in glucose uptake and lactate secretion, indicating their competitiveness in the uptake of glucose and the crucial early step of glycolysis, converting glucose to glucose-6-phosphate (although it seemed that myeloid cells showed the relatively lower expression of GLUT1, the average expression was low to neglect) (Figures 5A–5C). The key difference of transporter expression between tumor cells and myeloid cells was also

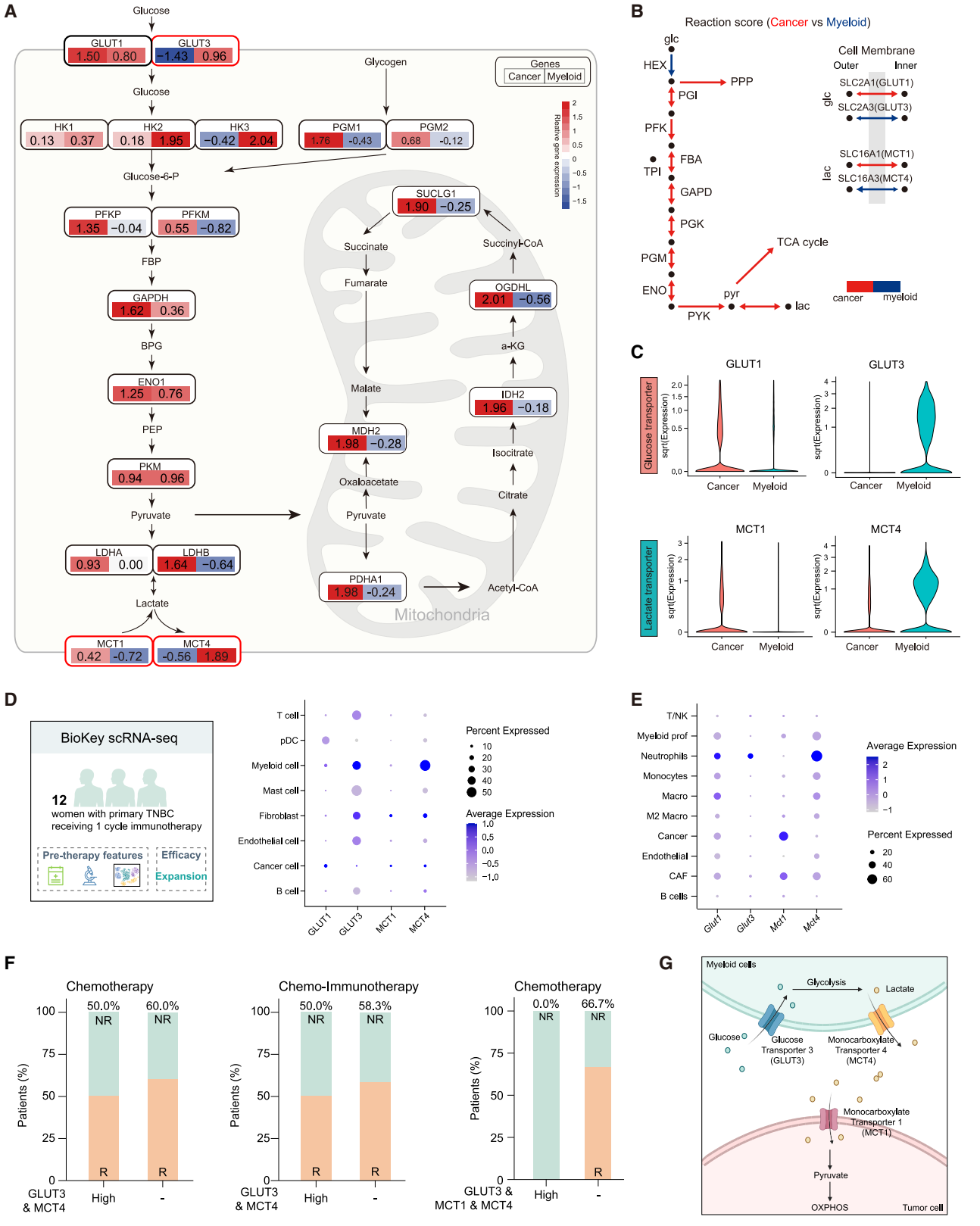

(legend on next page)

externally validated in the BioKey cohort and the mouse TNBC scRNA-seq cohort (Figures 5D and 5E). Additionally, the high expression of GLUT3 and MCT4 indicated the trend towards the worse chemotherapy and immunotherapy response (Figure 5F).

Based on these findings, we proposed a metabolic model wherein myeloid cells uptake glucose and secrete lactate by GLUT3 and MCT4, respectively, and tumor cells obtain the secreted lactate through MCT1 and utilize it as a substrate to sustain their growth (Figure 5G).

Tumor-myeloid cell crosstalk mediates the lactate re-use cycling to promote TNBC progression via the GLUT3/MCT1/MCT4 axis

To validate the hypothesis, we first verified the differential expression of GLUT3, MCT1, and MCT4 in both human and mouse TNBC tumor samples. Keeping in line with the preceding findings, multiplex immunofluorescence (mIF) staining in human samples, immunohistochemistry staining in mouse tumor tissues, and qPCR in mouse cell lines, confirmed that MCT4 and GLUT3 were predominantly expressed in myeloid cells, while MCT1 was mainly expressed in tumor cells (Figures 6A–6C).

Then, we explored whether these distinct expression patterns of GLUT3, MCT1, and MCT4 between cancer and myeloid cells directly affected the lactate flux and the growth of tumor cells. Therefore, we performed *in vitro* conditioned medium (CM) co-culture experiments. As for myeloid cells, knockdown of GLUT3 and MCT4, blocking the lactate production and export, inhibited the tumor cell growth and migration in the co-culture system (Figures 6D–6F). As for tumor cells, the knockdown of MCT1, which inhibited the import of lactate, could also impair the tumor cell progression in the co-culture system (Figures 6D and 6G). We also conducted a ^{13}C-based stable isotope labeling (SIL) experiment to validate that the knockdown of MCT1 decreased the uptake of ^{13}C-lactate and its conversion to ^{13}C labeled intermediate metabolites in the glycolysis and TCA cycle (Figure 6H). MCT1 inhibitor shows the same effect in *in vivo* and *in vitro* models (Figure 6I). Thus, both human and mouse cancer models confirmed that GLUT3- and MCT4-mediated glucose intake and lactate secretion in myeloid cells promoted the uptake and reuse of lactate in tumor cells, which ultimately promoted the tumor cell progression.

In general, we set an example from the comprehensive single-cell metabolic analysis to elucidate that the metabolic interaction between tumor and myeloid cells could promote TNBC progression.

MCT1 inhibitors in combination with ADC or immune checkpoint blockade as effective therapeutic strategies for TNBCs

We further explored the potential of targeting this metabolic crosstalk for optimizing existing TNBC treatment strategies. Given the specific expression of MCT1 in tumor cells and the accessibility of drug, we identified MCT1 as a promising therapeutic target, offering a strategy to disrupt the metabolic interactions that sustain tumor growth. The MCT1 inhibitor AZD3965 has also already completed a phase I clinical trial (NCT01791595) in patients with solid tumors and diffuse large B cell lymphoma.[31,32]

Given the clinical importance of Trop-2 ADCs in treating TNBC, approaches to improve tumor sensitivity to these agents have become a central area of ongoing clinical investigation. We sought to determine whether inhibiting lactate flux could sensitize tumors to SG *in vivo*. To this end, we generated stable MCT1-knockdown breast cancer cell lines and MCT4-knockdown myeloid cell lines to perform xenograft experiments. Knockdown of MCT1 in tumor cells and MCT4 in myeloid cells both enhanced the antitumor efficacy of SG (Figures 7A and S5A). At the pharmacologic level, while either MCT1 inhibitor or SG alone suppressed tumor growth, the combination treatment produced a more pronounced reduction in tumor burden compared with monotherapy (Figure 7B). Furthermore, we employed patient-derived xenograft (PDX) models to validate the combinatorial effect (Figure 7C). The results confirmed that MCT1 inhibition sensitizes TNBC to SG treatment, providing additional evidence supporting the potential *in vivo* therapeutic value of this combination strategy.

Next, we investigated whether inhibition of MCT could enhance the efficacy of immunotherapy. We established 4T1 orthotopic TNBC models and genetically suppressed MCT1 expression in 4T1 tumor cells and MCT4 expression in RAW264.7 myeloid cells. In both settings, inhibition of MCT1 or MCT4 sensitized tumors to immune checkpoint blockade (Figures 7D and S5B–S5D). Consistently, combination therapy with an MCT1 inhibitor and immunotherapy significantly enhanced antitumor activity compared with either monotherapy (Figures 7E–7G). To further dissect the immune response, we performed flow cytometry analysis of tumor-infiltrating immune cells following treatment. The combination regimen elicited a robust immune activation, increasing the proportions of $CD4^+$ T cells, $CD8^+$ T cells, PRF^+CD8^+ cytotoxic T cells, and $CD86^+$ macrophages, while simultaneously reducing $PD\text{-}1^+CD8^+$ T cells and $CD206^+$ macrophages (Figures 7H and 7I).

Figure 5. Distinct patterns of glucose utilization and lactate production in different microenvironmental cell types

(A) Diagram summarizing metabolic genes involved in glycolysis, TCA cycle, and glycogenolysis. Alterations are defined by significant upregulation or downregulation of mRNA expression in the scRNA-seq cohort. Alteration scores of each gene are depicted as the average mRNA expression in cancer cells and the myeloid cells.

(B) Metabolic maps showing metabolic reaction fluxes of glucose metabolism for cancer compared to myeloid cells.

(C) Violin plots showing the square-root expression of the crucial transporter genes between the cancer cells and myeloid cells.

(D-E) Dot plots showing the average expression and the percent of expressed cells of the transporter genes between microenvironment cells in the external human (D) and mouse cohort (E).

(F) Bar plots showing tumor responses to chemotherapy and immunotherapy after dichotomizing GLUT3–MCT4 and GLUT3–MCT1–MCT4 expression levels at the median. "High GLUT3 & MCT4 group" refers to cases in which both GLUT3 and MCT4 expression levels are higher in myeloid cells than in tumor cells, whereas "High GLUT3 & MCT1 & MCT4 group" indicates higher GLUT3 and MCT4 expression in myeloid cells and higher MCT1 expression in tumor cells.

(G) Conceptual basis of the immunometabolic crosstalk in our study.

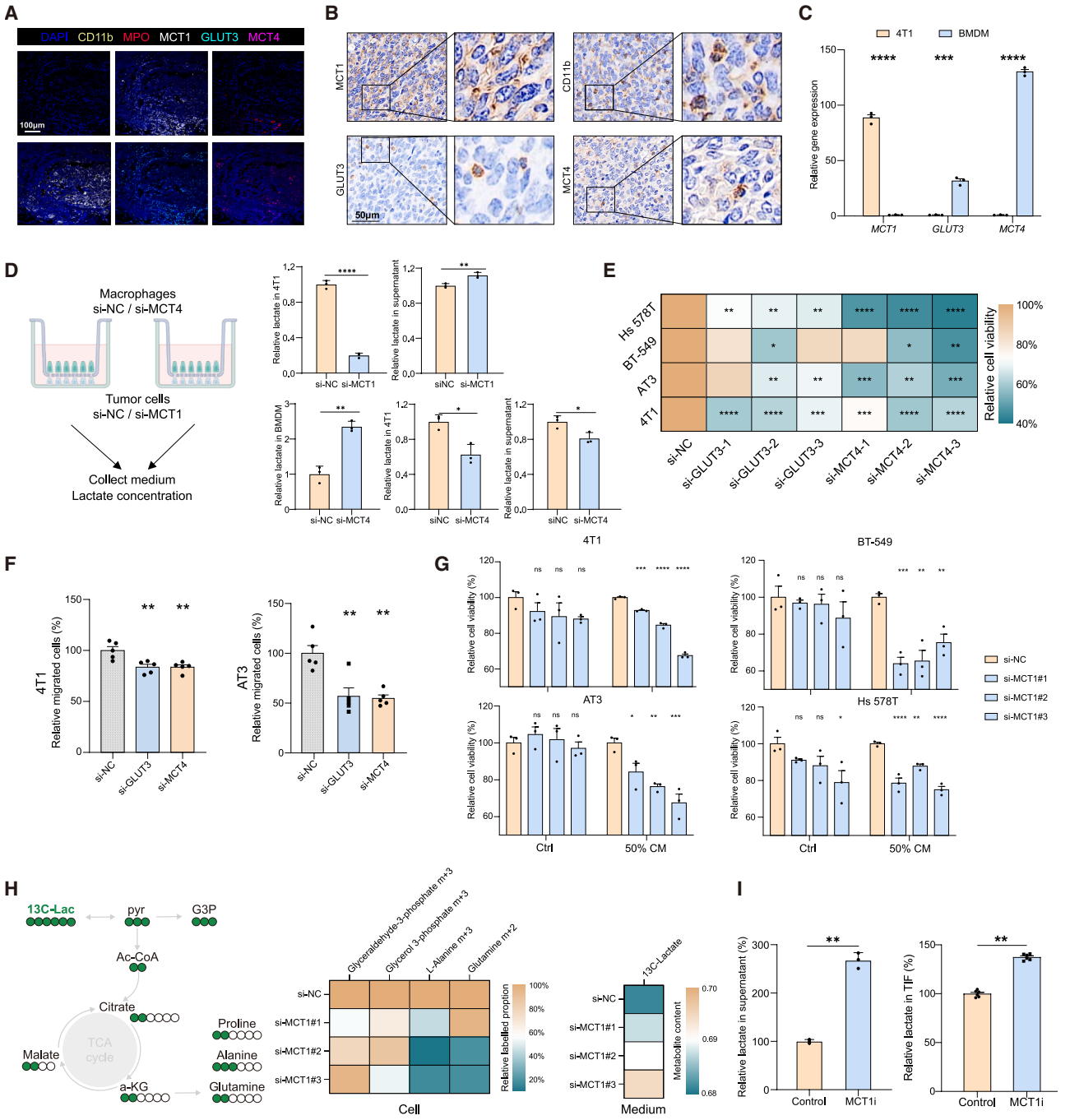

Figure 6. GLUT3/MCT1/MCT4 axis mediates the lactate re-use cycling to promote TNBC progression

(A) Multiple immunofluorescence analysis of CD11b, MPO, GLUT3, MCT1, and MCT4 expression in human TNBC tumor tissues. Scale bars, 100 μm.

(B) Immunohistochemistry analysis of CD11b, MCT1, MCT4, and GLUT3 expression in mouse 4T1 tumor tissues. Scale bars, 50 μm.

(C) Relative mRNA levels of MCT1, GLUT3, and MCT4 in 4T1 tumor cells and bone-marrow-derived macrophages (BMDMs). Data were compared using Student's *t* test ($n = 3$).

(D) Experimental design (left) and lactate levels in cell lysates and culture supernatants under si-NC or si-MCT1 tumor-cell conditions and si-NC or si-MCT4 BMDM conditions (right). Data were compared using Student's *t* test ($n = 3$).

(E) Cell growth assessment of tumor cells cultured in macrophage-conditioned medium from si-NC, si-GLUT3, and si-MCT4 cells after 24–48 h. Data were compared using one-way ANOVA test ($n = 3$).

(legend continued on next page)

In addition, we confirmed these findings in an AT3 syngeneic TNBC model, which similarly demonstrated enhanced antitumor responses following MCT inhibition combined with immunotherapy (Figures 7J–7N).

Our findings *in vivo* indicated that the combination of the MCT1 inhibitor with ADC or ICB holds significant promise as a therapeutic strategy in TNBC and warranted further clinical investigation.

DISCUSSION

The intricate metabolic interplay between tumor cells and other cells within the TME can profoundly influence therapeutic response and resistance mechanisms, thereby affecting treatment outcomes in TNBC.[33,34] By leveraging the scRNA-seq technologies and multidimensional metabolic analyses, we systematically provided a comprehensive and systematic portrayal of the single-cell metabolic landscape within the TNBC ecosystem. Specifically, our investigation into the potential association with chemotherapy and immunotherapy response yielded a pivotal finding. As an illustrative example of our single-cell metabolic analysis, we found that differential expression of glycol-metabolic transporters like MCT4, MCT1, and GLUT3 among microenvironmental cells facilitated tumor progression. This discovery opens promising possibilities for the development of combination therapies that incorporate MCT1 inhibitors along with ADC therapy or immunotherapy for TNBC, potentially enhancing treatment efficacy and patient outcomes.

Compared with previous studies focusing on bulk tumor metabolism, we leveraged a single-cell TNBC cohort to resolve microenvironmental metabolic features at high resolution and to identify key cell-type-specific metabolic traits and their potential interplay associated with treatment response. Previous studies often embarked directly from differentially expressed metabolic enzymes or metabolites and subsequently identified related cell types. Next, by detecting upstream and downstream metabolic pathways, these studies aimed to elucidate the impact of metabolic processes on tumor biological behavior or treatment response.[35–37] Based on integrated metabolomic and transcriptomic analyses, Li et al. identified N-acetylaspartate (NAA) and its synthetase N-acetyltransferase 8-like (NAT8L) as efficacy-related metabolic determinants. Upon confirming their high expression in tumor cells, researchers further delineated the mechanistic basis by which this metabolite contributes to immunotherapy resistance.[35] This paradigm failed to gain a comprehensive understanding of overall metabolic characteristics within the microenvironment. In order to overcome this limitation, we systematically analyzed the metabolic characteristics of the TNBC microenvironment and portrayed gradually deepening atlas at single-cell level. First, we verified and displayed the metabolic heterogeneity of different cell types in details. Second, the metabolic traits of different cells and their correlation with treatment response were explored in depth. Finally, we focused on interesting specificity of differential carbohydrate transporter expression in TNBC, for which we conducted experimental verification and clinical translation. Therefore, our study represents a paradigm shift in the field of immunometabolism and serves as a reference for future analytical research endeavors.

Regarding the specific metabolic analytical methodology, we innovatively integrated the scRNA-seq and multidimensional metabolic analytical tools to unveil a high-resolution and high-precision single-cell metabolic landscape, enriching our understanding of metabolic dysregulation in TNBC and potentially other cancers. The resolution of conventional multi-omics tools like bulk RNA-seq is too low to decipher the cell-type-specific metabolic characteristics and potential interactions. Thus, it is necessary to expand the scope and improve the accuracy of metabolic analysis to target cancer metabolism in the era of precision oncology. The advent of scRNA-seq and FBA analysis widely expanded the current research. Remarkably, our approach extended beyond the examination of metabolic genes and pathways, as we ventured into flux balance analysis by Compass to predict the flow of metabolic changes. By harnessing these advanced technologies and methodologies, we have not only refined our comprehension of cell-type-specific metabolic characteristics but also emphasized the superiority of the combination of cell types and metabolic features over merely cell type or bulk metabolic features. The intricate metabolic interactions between tumor cells and other cells in the TME have been extensively demonstrated to exert a significant influence on the response to chemotherapy and immunotherapy. Common metabolic crosstalk modes mainly include nutrient competition, immune-modulatory effects of metabolites, and metabolic adaptability. Specifically, cancer cells have been shown to engage in a cooperative or competitive metabolic relationship with microenvironment cells, aiming to secure essential nutrients for their rapid proliferation while hindering antitumor responses.[38] For example, the ‘‘host-parasite relationship’’ between catabolic CAFs and anabolic cancer cells confers latter with chemotherapy resistance.[39] Tumor cells exhibit heightened expression of the methionine transporter SLC43A2, thereby outcompeting T cells for methionine, a crucial amino acid, to foster their own growth and dampen antitumor immunity.[40] Lactate, the crucial metabolite in our study, has been widely associated with cancer progression and therapeutic resistance.[41–44] Previous studies have demonstrated its effects on the physical properties of TME and its direct impact on the metabolism of individual cell types.[45–47] Our study further expands this perspective by investigating lactate’s role as a carbon

(F) Cell migration assessment of 4T1 and AT3 tumor cells cultured in macrophage-conditioned medium from si-NC, si-GLUT3, and si-MCT4 cells. Data were compared using one-wayANOVA test ($n = 5$).
(G) Cell growth assessment of si-NC and si-MCT1 tumor cells cultured in macrophages conditioned medium. Data were compared using one-way ANOVA test ($n = 3$).
(H) ^{13}C-labeling of glucose trancing of TCA cycle associated metabolites and lactate levels in the culture medium.
(I) Relative lactate concentration in the co-culture medium ($n = 3$) and tissue interstitial fluid ($n = 6$) after MCT1 inhibitor treatment.
The data are presented as the mean ± SEM. ****$p < 0.0001$; ***$p < 0.001$; **$p < 0.01$; *$p < 0.05$; ns, $p \geq 0.05$.

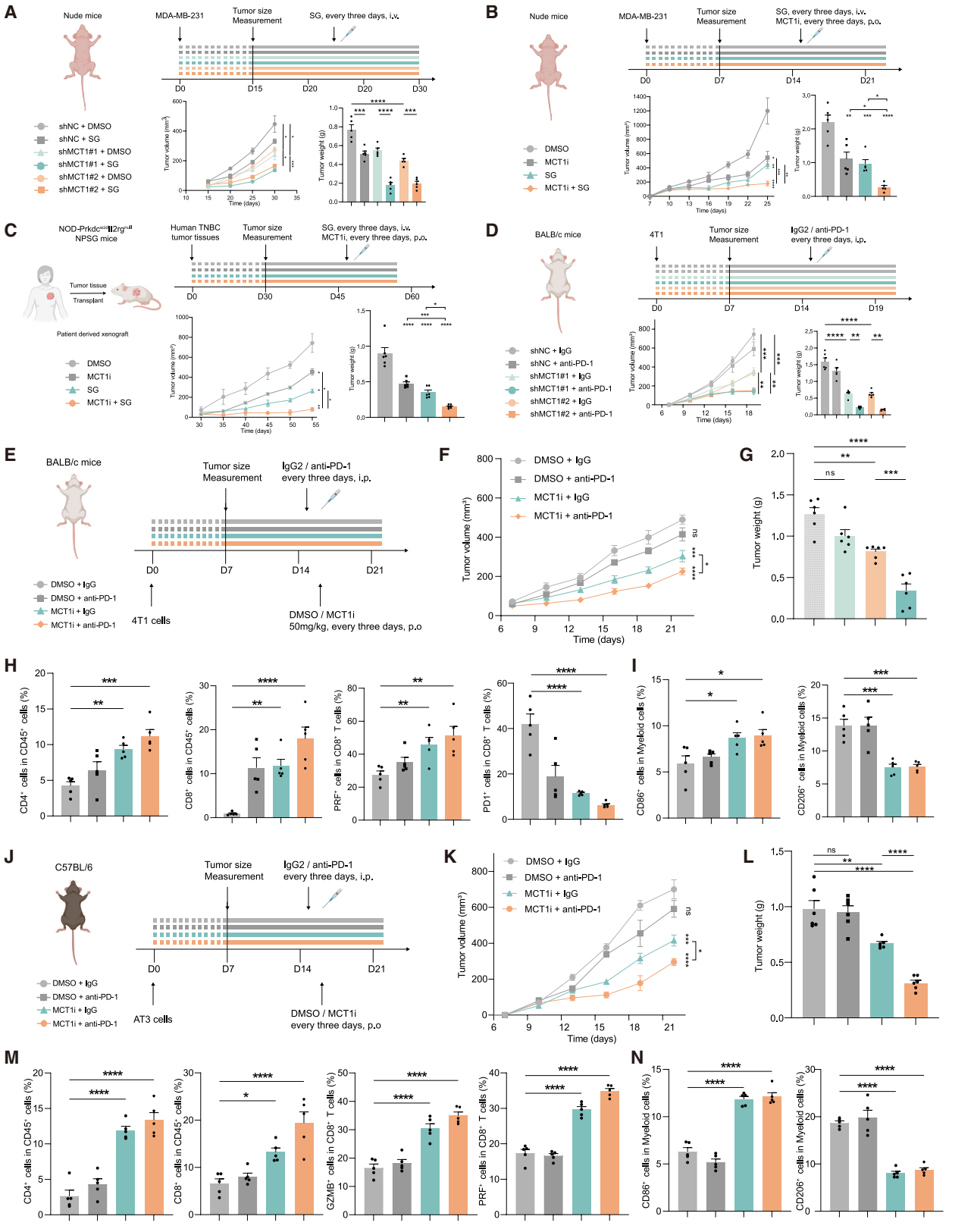

(legend on next page)

source that shapes metabolic crosstalk and highlights lactate transport within the TME as a promising therapeutic target. Reinfeld et al. demonstrated that myeloid cells represent the most avid glucose-consuming population within the TME and exhibit a higher basal extracellular acidification rate compared to tumor-infiltrating T cells and cancer cells.[48] Consistent with these observations, our single-cell transcriptomic analysis revealed elevated expression of GLUT3 in myeloid cells, providing a potential mechanistic basis for their heightened glucose uptake. Moreover, through both *in vitro* co-culture systems and *in vivo* genetic models, we demonstrated that lactate secreted by myeloid cells via MCT4 can enhance the malignant biological behavior of cancer.

In addition to glucose-lactate metabolism, metabolic reprogramming of lipids and amino acids has also been discussed in TNBC. Yu et al. reported that tumor-derived extracellular vesicles laden with lipids mediate neutrophil reprogramming, thereby promoting TNBC cells survival following immunotherapy and chemotherapy.[49] Separate lines of evidence implicate amino acids, including glutamine and arginine, as critical players in TNBC progression.[50,51] Corroborating the role of metabolic rewiring in TME, our analysis revealed an association between lipid metabolic pathways/gene expression in myeloid cells and response to immunotherapy or chemotherapy. Therefore, mechanistic investigations into these additional metabolic features found from the cohort also represent a meaningful direction.

Specifically, MCT4 and MCT1 stand out as possible therapeutic targets due to their central roles in lactate shuttling. MCT4 primarily exports intracellular lactate into the extracellular space, while MCT1 functions as the main lactate importer in tumor cells. Advances in understanding the regulatory mechanisms of MCTs have paved the way for the rational design and clinical development of inhibitors. A noteworthy example is the MCT1 inhibitor AZD3965, which has been proved to enhance the efficacy of chemotherapy and immunotherapy against various types of cancer by inducing intracellular lactate accumulation.[32,52,53] Beyond its direct effects on cancer cells, MCT1 inhibition can modulate the tumor immune microenvironment to enhance anti-tumor immunity. Kumagai et al. demonstrated that the inhibition of MCT1 of regulatory T (Treg) cells reduced the frequency of Treg cells and their PD-1 expression, leading to a significant inhibition of tumor growth by anti-PD-1 therapy.[54] And the work of Niveau et al. showed that blockade of the MCT1 transporter can rescue conventional dendritic cells from glycan-induced functional hijacking and further restore anti-tumor T cell fitness.[55] In addition to its synergy with immune checkpoint inhibitors, Lopez et al. identified enhanced cytotoxicity *in vitro* and improved antitumoral control *in vivo* when MCT1 blockade was combined with CAR T cell therapy, indicating the potential of combining MCT1 inhibitors with other immunotherapies.[56] Similarly, the potent MCT4 inhibitor VB124 improves anti-PD-1 therapy in hepatocellular carcinoma xenografts.[57] Syrosingopine, an orally bioavailable dual MCT1 and MCT4 inhibitor, demonstrates enhanced anticancer effects in breast cancer and adult T cell leukemia.[58,59] Although initial studies have explored combining MCT inhibition with other therapies using conventional molecular biology models, the expression patterns, specific functional roles, and therapeutic impact of MCTs across diverse cell types in the TME at single-cell resolution have remained unclear. This knowledge gap has contributed to excessive off-target effects and toxicity, limiting broader clinical application.[60] Meanwhile, the emergence of targeted agents, such as ADCs and anti-angiogenic drugs, has further expanded the applicability of metabolism-targeted combination therapies. Whereas MCT4-selective inhibitors (e.g., MSC-4381, AZ1422, and AZD0095) remain confined to pre-clinical evaluation and retain unresolved biosafety and efficacy liabilities, MCT1-targeted compounds like AZD3965 are already clinically accessible and pharmacologically optimized.[61–63] Building on this, our study systematically analyzed the single-cell expression pattern of MCT among TME and provided *in vivo* evidence validating the synergistic antitumor effects of combining MCT1 inhibition with ADC or ICB. Together, our findings underscore the promise of integrating lactate transport blockade with existing immunotherapies or targeted agents to improve clinical outcomes in TNBC. It is worth mentioning that while our scRNA-seq analysis revealed that MCT1 expression is highest in tumor cells compared to other cell types, our experimental results cannot exclude the possibility that MCT1 inhibitors exert anti-tumor effects by targeting other cells in the microenvironment.

Moreover, our study has several important implications for clinical translations. SG is a humanized Trop-2-specific

Figure 7. MCT1 inhibitor enhances anti-Trop2 and immunotherapy efficacy in TNBC

(A) Study design, growth curves, and tumor weights to observe whether knockdown of MCT1 could affect the sensitivity to sacituzumab govitecan, SG ($n = 5$).
(B) Study design, growth curves, and tumor weights to observe whether MCT1 inhibitor could improve the sensitivity to sacituzumab govitecan ($n = 5$).
(C) Study design, growth curves, and tumor weights to observe whether MCT1 inhibitor could improve the sensitivity to sacituzumab govitecan in human TNBC PDX tumors treated as indicated ($n = 6$).
(D) Study design, growth curves, and tumor weights to observe whether shMCT1 could affect the sensitivity to immunotherapy ($n = 5$).
(E–G) Study design (E), growth curves (F), and tumor weights (G) to observe whether MCT1 inhibitor could affect the sensitivity to immunotherapy in 4T1 tumors ($n = 6$).
(H–I) Bar plots showing the percentage of $CD4^+$ cells among $CD45^+$ cells, $CD8^+$ cells among $CD45^+$ cells, PRF^+ cells among $CD8^+$ T cells, $PD1^+$ cells among $CD8^+$ T cells, $CD86^+$ cells among myeloid cells, and $CD206^+$ cells among myeloid cells in tumors (upper) measured using flow cytometry. The data are presented as the mean ± SEM. Data were compared using one-way ANOVA.
(J–L) Study design (J), growth curves (K), and tumor weights (L) to observe whether MCT1 inhibitor could affect the sensitivity to immunotherapy in AT3 tumors ($n = 6$).
(M and N) Bar plots showing the percentage of $CD4^+$ cells among $CD45^+$ cells, $CD8^+$ cells among $CD45^+$ cells, PRF^+ cells among $CD8^+$ T cells, $GZMB^+$ cells among $CD8^+$ T cells, $CD86^+$ cells among myeloid cells, and $CD206^+$ cells among myeloid cells in tumors (upper) measured using flow cytometry. The data are presented as the mean ± SEM. Data were compared using one-way ANOVA.
$^{****}p < 0.0001$; $^{***}p < 0.001$; $^{**}p < 0.01$; $^{*}p < 0.05$; ns, $p \geq 0.05$.

antibody linked to the active irinotecan metabolite SN-38.[64] Trials like NeoSTAR and ASCENT demonstrated its efficacy and feasibility for localized and metastatic breast cancer, respectively, moving SG toward the later-line treatment of TNBC.[65,66] However, resistance to sacituzumab govitecan can still develop, which may be partly due to loss of Trop-2 expression or mutations affecting its function, as reported in previous studies.[67] Immunotherapy is another promising therapy in TNBC. Trials like the KEYNOTE-522 and KEYNOTE-355 pointed to efficacy and prognostic benefit with the addition of immunotherapy to traditional chemotherapy backbone in TNBCs.[68,69] However, the low objective response rate, unique immune-related toxicities, hyper-progression, and lack of promising predictive markers for effectiveness can sometimes hinder the generalization of immunotherapy.[70] Given the specific expression of MCT1 in tumor cells and the accessibility of drug, we identified MCT1 as a promising therapeutic target. In our study, the combination of a MCT1 inhibitor with SG or anti-PD-1 efficiently impaired the tumor growth *in vivo*, which provides a rationale to explore the application of MCT1 inhibitors as anti-tumor synergistic agents for both ADC and immunotherapy. Besides, despite limitations of cohort size, the baseline expression of GLUT3, MCT1, and MCT4 may effectively predict the response to chemotherapy. Future studies into the precise therapies for patients with high baseline expression of GLUT3, MCT1, and MCT4 should be explored.

In conclusion, our study provided a comprehensive single-cell metabolic atlas and suggested a paradigm shift in the understanding of metabolic crosstalk within the TME at the single-cell level. On this basis, we explored the specific metabolic targets to sensitize TNBC to chemotherapy and immunotherapy and demonstrated that the combining MCT1 inhibitors with ICB and SG is an optimal therapy for TNBC patients awaiting clinical validation.

Limitations of the study

Our study has several limitations. First, given the inherent complexity of metabolic regulation, analyses based solely on transcriptional profiles may introduce informational bias. Although independent cohort validation and metabolic assays support our conclusions, multi-omics and functional studies are warranted. Second, due to the sample size of cohorts and sex composition in this study, some observations, like the contributions of other cell populations in lactate reflux and efficacy association should be interpreted cautiously and validated in larger datasets. Finally, although our preclinical models provide mechanistic evidence, *in vivo* experiments are limited to evaluations of tumor growth and alterations in the TME. The survival outcomes as well as the efficacy of MCT1 inhibition combined with chemo-immunotherapy require further investigation before clinical translation.

RESOURCE AVAILABILITY

Lead contact

Further information and requests for resources or reagents should be directed to and will be fulfilled by the lead contact, Prof. Yi-Zhou Jiang (yizhoujiang@fudan.edu.cn).

Materials availability

This study did not generate any novel reagents. Patient materials described in this manuscript should be requested directly from the lead contact and will be considered on an individual basis due to ethics and patient consent.

Data and code availability

- Single-cell RNA-seq data of this study is accessible in The National Omics Data Encyclopedia:OEP003394. The raw FASTQ files in this study will be provided for scientific research upon request complying with the law due to human patient privacy concerns. The scRNA-seq data of 4T1 orthotopic tumors were obtained from a previously published study and are available at the Dryad data repository (https://datadryad.org). Cell-type information provided in the attached metadata was directly used for downstream analyses.[17] scRNA-seq data and human metadata of the Biokey cohort are available at the European Genome-phenome Archive: EGAS00001004809. The sequencing data of the I-SPY2 cohort (only TNBC samples were included) is available in the GEO datasets: GSE173839.
- Our study does not report custom computer code.
- Any additional information required to reanalyze the data reported in this paper is available from the lead contact upon request.

ACKNOWLEDGMENTS

This work was supported by grants from the National Natural Science Foundation of China (82441028, 82573645), "Clinical Cohort Shanghai" (No. SHDC2025CCS018), the Fundamental and Interdisciplinary Disciplines Breakthrough Plan of the Ministry of Education of China (JYB2025XDXM611), and the HE Research Fellowships from the HE Science Foundation,. Y.-Z.J. is a SANS Exploration Scholar. The funders had no role in the study design, data collection and analysis, decision to publish, or preparation of the manuscript.

AUTHOR CONTRIBUTIONS

Conceptualization, Y.X., Y.-Z.J., and Z.-M.S. Methodology, Y. Xu., X.-Y.L., H.Z., and H.W. Data curation, Y.X., L.C., Y. Xu., and X.-Y.L. Formal analysis, Y. Xu and X.-Y.L. Visualization, Y. Xu and X.-Y.L. Experiment, Y. Xu and X.-Y.L. Writing—original draft, Y. Xu, X.-Y.L., H.W., and Y.X. Project administration, Y. Xu., X.-Y.L, H.W., Y.X., Z.-M.S., and Y.-Z.J. Supervision, Y.X., Z.-M.S., and Y.-Z.J.

DECLARATION OF INTERESTS

The authors declare no competing interests.

STAR★METHODS

Detailed methods are provided in the online version of this paper and include the following:

- KEY RESOURCES TABLE
- EXPERIMENTAL MODEL AND STUDY PARTICIPANT DETAILS
  - Patients and clinical samples
  - Human and mouse TNBC cell lines
  - Murine models
  - Human and mouse myeloid cells preparation
  - *In vivo* mouse studies
- METHOD DETAILS
  - scRNA-seq data pre-processing and quality control
  - Visualization and clustering
  - Cell type annotation
  - Metabolic gene sets construction
  - Differentially expressed metabolic genes analysis
  - Calculation of metabolic pathway activities
  - Compass analysis
  - Single-cell metabolic features-treatment interaction analysis
  - Multiplex immunofluorescence staining

- Immunohistochemical staining
- Stable isotope labeling (SIL) and metabolomics
- RNA isolation and quantitative real-time PCR (qRT-PCR)
- Transfection of small interfering RNAs
- *In vitro* cell viability assays
- *In vitro* cell migration and invasion assays
- Flow cytometry analysis

- QUANTIFICATION AND STATISTICAL ANALYSIS

SUPPLEMENTAL INFORMATION

Supplemental information can be found online at https://doi.org/10.1016/j.xcrm.2026.102659.

Received: February 7, 2025
Revised: December 17, 2025
Accepted: February 6, 2026
Published: March 17, 2026

REFERENCES

1. Masuda, H., Brewer, T.M., Liu, D.D., Iwamoto, T., Shen, Y., Hsu, L., Willey, J.S., Gonzalez-Angulo, A.M., Chavez-MacGregor, M., Fouad, T.M., et al. (2014). Long-term treatment efficacy in primary inflammatory breast cancer by hormonal receptor- and HER2-defined subtypes. Ann. Oncol. *25*, 384–391. https://doi.org/10.1093/annonc/mdt525.
2. Bianchini, G., Balko, J.M., Mayer, I.A., Sanders, M.E., and Gianni, L. (2016). Triple-negative breast cancer: challenges and opportunities of a heterogeneous disease. Nat. Rev. Clin. Oncol. *13*, 674–690. https://doi.org/10.1038/nrclinonc.2016.66.
3. Khoury, R., Saleh, K., Khalife, N., Saleh, M., Chahine, C., Ibrahim, R., and Lecesne, A. (2023). Mechanisms of Resistance to Antibody-Drug Conjugates. Int. J. Mol. Sci. *24*, 9674. https://doi.org/10.3390/ijms24119674.
4. Pusztai, L., Karn, T., Safonov, A., Abu-Khalaf, M.M., and Bianchini, G. (2016). New Strategies in Breast Cancer: Immunotherapy. Clin. Cancer Res. *22*, 2105–2110. https://doi.org/10.1158/1078-0432.Ccr-15-1315.
5. Jiang, Z., Ouyang, Q., Sun, T., Zhang, Q., Teng, Y., Cui, J., Wang, H., Yin, Y., Wang, X., Zhou, X., et al. (2024). Toripalimab plus nab-paclitaxel in metastatic or recurrent triple-negative breast cancer: a randomized phase 3 trial. Nat. Med. *30*, 249–256. https://doi.org/10.1038/s41591-023-02677-x.
6. Sharma, P., Stecklein, S.R., Yoder, R., Staley, J.M., Schwensen, K., O'Dea, A., Nye, L., Satelli, D., Crane, G., Madan, R., et al. (2024). Clinical and Biomarker Findings of Neoadjuvant Pembrolizumab and Carboplatin Plus Docetaxel in Triple-Negative Breast Cancer: NeoPACT Phase 2 Clinical Trial. JAMA Oncol. *10*, 227–235. https://doi.org/10.1001/jamaoncol.2023.5033.
7. Mittendorf, E.A., Zhang, H., Barrios, C.H., Saji, S., Jung, K.H., Hegg, R., Koehler, A., Sohn, J., Iwata, H., Telli, M.L., et al. (2020). Neoadjuvant atezolizumab in combination with sequential nab-paclitaxel and anthracycline-based chemotherapy versus placebo and chemotherapy in patients with early-stage triple-negative breast cancer (IMpassion031): a randomised, double-blind, phase 3 trial. Lancet *396*, 1090–1100. https://doi.org/10.1016/s0140-6736(20)31953-x.
8. Schmid, P., Cortes, J., Dent, R., Pusztai, L., McArthur, H., Kümmel, S., Bergh, J., Denkert, C., Park, Y.H., Hui, R., et al. (2022). Event-free Survival with Pembrolizumab in Early Triple-Negative Breast Cancer. N. Engl. J. Med. *386*, 556–567. https://doi.org/10.1056/NEJMoa2112651.
9. Adams, S., Schmid, P., Rugo, H.S., Winer, E.P., Loirat, D., Awada, A., Cescon, D.W., Iwata, H., Campone, M., Nanda, R., et al. (2019). Pembrolizumab monotherapy for previously treated metastatic triple-negative breast cancer: cohort A of the phase II KEYNOTE-086 study. Ann. Oncol. *30*, 397–404. https://doi.org/10.1093/annonc/mdy517.
10. Adams, S., Loi, S., Toppmeyer, D., Cescon, D.W., De Laurentiis, M., Nanda, R., Winer, E.P., Mukai, H., Tamura, K., Armstrong, A., et al. (2019). Pembrolizumab monotherapy for previously untreated, PD-L1-positive, metastatic triple-negative breast cancer: cohort B of the phase II KEYNOTE-086 study. Ann. Oncol. *30*, 405–411. https://doi.org/10.1093/annonc/mdy518.
11. Keenan, T.E., and Tolaney, S.M. (2020). Role of Immunotherapy in Triple-Negative Breast Cancer. J. Natl. Compr. Cancer Netw. *18*, 479–489. https://doi.org/10.6004/jnccn.2020.7554.
12. Orth, J.D., Thiele, I., and Palsson, B.Ø. (2010). What is flux balance analysis? Nat. Biotechnol. *28*, 245–248. https://doi.org/10.1038/nbt.1614.
13. Oberhardt, M.A., Chavali, A.K., and Papin, J.A. (2009). Flux balance analysis: interrogating genome-scale metabolic networks. Methods Mol. Biol. *500*, 61–80. https://doi.org/10.1007/978-1-59745-525-1_3.
14. Alghamdi, N., Chang, W., Dang, P., Lu, X., Wan, C., Gampala, S., Huang, Z., Wang, J., Ma, Q., Zang, Y., et al. (2021). A graph neural network model to estimate cell-wise metabolic flux using single-cell RNA-seq data. Genome Res. *31*, 1867–1884. https://doi.org/10.1101/gr.271205.120.
15. Wagner, A., Wang, C., Fessler, J., DeTomaso, D., Avila-Pacheco, J., Kaminski, J., Zaghouani, S., Christian, E., Thakore, P., Schellhaass, B., et al. (2021). Metabolic modeling of single Th17 cells reveals regulators of autoimmunity. Cell *184*, 4168–4185.e21. https://doi.org/10.1016/j.cell.2021.05.045.
16. Xiao, Y., Yu, T.J., Xu, Y., Ding, R., Wang, Y.P., Jiang, Y.Z., and Shao, Z.M. (2023). Emerging therapies in cancer metabolism. Cell Metab. *35*, 1283–1303. https://doi.org/10.1016/j.cmet.2023.07.006.
17. Sebastian, A., Hum, N.R., Martin, K.A., Gilmore, S.F., Peran, I., Byers, S.W., Wheeler, E.K., Coleman, M.A., and Loots, G.G. (2020). Single-Cell Transcriptomic Analysis of Tumor-Derived Fibroblasts and Normal Tissue-Resident Fibroblasts Reveals Fibroblast Heterogeneity in Breast Cancer. Cancers (Basel) *12*, 1307. https://doi.org/10.3390/cancers12051307.
18. Bassez, A., Vos, H., Van Dyck, L., Floris, G., Arijs, I., Desmedt, C., Boeckx, B., Vanden Bempt, M., Nevelsteen, I., Lambein, K., et al. (2021). A single-cell map of intratumoral changes during anti-PD1 treatment of patients with breast cancer. Nat. Med. *27*, 820–832. https://doi.org/10.1038/s41591-021-01323-8.
19. Wu, S.Z., Al-Eryani, G., Roden, D.L., Junankar, S., Harvey, K., Andersson, A., Thennavan, A., Wang, C., Torpy, J.R., Bartonicek, N., et al. (2021). A single-cell and spatially resolved atlas of human breast cancers. Nat. Genet. *53*, 1334–1347. https://doi.org/10.1038/s41588-021-00911-1.
20. Hollern, D.P., Xu, N., Thennavan, A., Glodowski, C., Garcia-Recio, S., Mott, K.R., He, X., Garay, J.P., Carey-Ewend, K., Marron, D., et al. (2019). B Cells and T Follicular Helper Cells Mediate Response to Checkpoint Inhibitors in High Mutation Burden Mouse Models of Breast Cancer. Cell *179*, 1191–1206.e21. https://doi.org/10.1016/j.cell.2019.10.028.
21. Wolf, D.M., Yau, C., Wulfkuhle, J., Brown-Swigart, L., Gallagher, R.I., Lee, P.R.E., Zhu, Z., Magbanua, M.J., Sayaman, R., O'Grady, N., et al. (2022). Redefining breast cancer subtypes to guide treatment prioritization and maximize response: Predictive biomarkers across 10 cancer therapies. Cancer Cell *40*, 609–623.e6. https://doi.org/10.1016/j.ccell.2022.05.005.
22. Xiao, Z., Dai, Z., and Locasale, J.W. (2019). Metabolic landscape of the tumor microenvironment at single cell resolution. Nat. Commun. *10*, 3763. https://doi.org/10.1038/s41467-019-11738-0.
23. Lee, J.W., Su, Y., Baloni, P., Chen, D., Pavlovitch-Bedzyk, A.J., Yuan, D., Duvvuri, V.R., Ng, R.H., Choi, J., Xie, J., et al. (2022). Integrated analysis of plasma and single immune cells uncovers metabolic changes in individuals with COVID-19. Nat. Biotechnol. *40*, 110–120. https://doi.org/10.1038/s41587-021-01020-4.
24. Iwamoto, H., Abe, M., Yang, Y., Cui, D., Seki, T., Nakamura, M., Hosaka, K., Lim, S., Wu, J., He, X., et al. (2018). Cancer Lipid Metabolism Confers Antiangiogenic Drug Resistance. Cell Metab. *28*, 104–117.e5. https://doi.org/10.1016/j.cmet.2018.05.005.
25. Liu, L., Mo, M., Chen, X., Chao, D., Zhang, Y., Chen, X., Wang, Y., Zhang, N., He, N., Yuan, X., et al. (2023). Targeting inhibition of prognosis-related lipid metabolism genes including CYP19A1 enhances immunotherapeutic

response in colon cancer. J. Exp. Clin. Cancer Res. *42*, 85. https://doi.org/10.1186/s13046-023-02647-8.

26. Veglia, F., Tyurin, V.A., Blasi, M., De Leo, A., Kossenkov, A.V., Donthireddy, L., To, T.K.J., Schug, Z., Basu, S., Wang, F., et al. (2019). Fatty acid transport protein 2 reprograms neutrophils in cancer. Nature *569*, 73–78. https://doi.org/10.1038/s41586-019-1118-2.

27. Zhang, W., Dai, J., Hou, G., Liu, H., Zheng, S., Wang, X., Lin, Q., Zhang, Y., Lu, M., Gong, Y., et al. (2023). SMURF2 predisposes cancer cell toward ferroptosis in GPX4-independent manners by promoting GSTP1 degradation. Mol. Cell *83*, 4352–4369.e8. https://doi.org/10.1016/j.molcel.2023.10.042.

28. Li, J., Zheng, C., Mai, Q., Huang, X., Pan, W., Lu, J., Chen, Z., Zhang, S., Zhang, C., Huang, H., et al. (2023). Tyrosine catabolism enhances genotoxic chemotherapy by suppressing translesion DNA synthesis in epithelial ovarian cancer. Cell Metab. *35*, 2044–2059.e8. https://doi.org/10.1016/j.cmet.2023.10.002.

29. Shi, Q., Shen, Q., Liu, Y., Shi, Y., Huang, W., Wang, X., Li, Z., Chai, Y., Wang, H., Hu, X., et al. (2022). Increased glucose metabolism in TAMs fuels O-GlcNAcylation of lysosomal Cathepsin B to promote cancer metastasis and chemoresistance. Cancer Cell *40*, 1207–1222.e10. https://doi.org/10.1016/j.ccell.2022.08.012.

30. Zhang, S., Zhang, Y., Feng, Y., Wu, J., Hu, Y., Lin, L., Xu, C., Chen, J., Tang, Z., Tian, H., and Chen, X. (2022). Biomineralized Two-Enzyme Nanoparticles Regulate Tumor Glycometabolism Inducing Tumor Cell Pyroptosis and Robust Antitumor Immunotherapy. Adv. Mater. *34*, e2206851. https://doi.org/10.1002/adma.202206851.

31. Halford, S., Veal, G.J., Wedge, S.R., Payne, G.S., Bacon, C.M., Sloan, P., Dragoni, I., Heinzmann, K., Potter, S., Salisbury, B.M., et al. (2023). A Phase I Dose-escalation Study of AZD3965, an Oral Monocarboxylate Transporter 1 Inhibitor, in Patients with Advanced Cancer. Clin. Cancer Res. *29*, 1429–1439. https://doi.org/10.1158/1078-0432.Ccr-22-2263.

32. Noble, R.A., Bell, N., Blair, H., Sikka, A., Thomas, H., Phillips, N., Nakjang, S., Miwa, S., Crossland, R., Rand, V., et al. (2017). Inhibition of monocarboxyate transporter 1 by AZD3965 as a novel therapeutic approach for diffuse large B-cell lymphoma and Burkitt lymphoma. Haematologica *102*, 1247–1257. https://doi.org/10.3324/haematol.2016.163030.

33. Xia, L., Oyang, L., Lin, J., Tan, S., Han, Y., Wu, N., Yi, P., Tang, L., Pan, Q., Rao, S., et al. (2021). The cancer metabolic reprogramming and immune response. Mol. Cancer *20*, 28. https://doi.org/10.1186/s12943-021-01316-8.

34. Leone, R.D., and Powell, J.D. (2020). Metabolism of immune cells in cancer. Nat. Rev. Cancer *20*, 516–531. https://doi.org/10.1038/s41568-020-0273-y.

35. Li, Y., Huang, M., Wang, M., Wang, Y., Deng, P., Li, C., Huang, J., Chen, H., Wei, Z., Ouyang, Q., et al. (2024). Tumor cells impair immunological synapse formation via central nervous system-enriched metabolite. Cancer Cell *42*, 985–1002.e18. https://doi.org/10.1016/j.ccell.2024.05.006.

36. Sun, Y., Zhang, X., Hang, D., Lau, H.C.H., Du, J., Liu, C., Xie, M., Pan, Y., Wang, L., Liang, C., et al. (2024). Integrative plasma and fecal metabolomics identify functional metabolites in adenoma-colorectal cancer progression and as early diagnostic biomarkers. Cancer Cell *42*, 1386–1400.e8. https://doi.org/10.1016/j.ccell.2024.07.005.

37. Zhou, P., Chang, W.Y., Gong, D.A., Xia, J., Chen, W., Huang, L.Y., Liu, R., Liu, Y., Chen, C., Wang, K., et al. (2023). High dietary fructose promotes hepatocellular carcinoma progression by enhancing O-GlcNAcylation via microbiota-derived acetate. Cell Metab. *35*, 1961–1975.e6. https://doi.org/10.1016/j.cmet.2023.09.009.

38. Kaymak, I., Williams, K.S., Cantor, J.R., and Jones, R.G. (2021). Immunometabolic Interplay in the Tumor Microenvironment. Cancer Cell *39*, 28–37. https://doi.org/10.1016/j.ccell.2020.09.004.

39. Yu, T., Yang, G., Hou, Y., Tang, X., Wu, C., Wu, X.A., Guo, L., Zhu, Q., Luo, H., Du, Y.E., et al. (2017). Cytoplasmic GPER translocation in cancer-associated fibroblasts mediates cAMP/PKA/CREB/glycolytic axis to confer tumor cells with multidrug resistance. Oncogene *36*, 2131–2145. https://doi.org/10.1038/onc.2016.370.

40. Bian, Y., Li, W., Kremer, D.M., Sajjakulnukit, P., Li, S., Crespo, J., Nwosu, Z.C., Zhang, L., Czerwonka, A., Pawłowska, A., et al. (2020). Cancer SLC43A2 alters T cell methionine metabolism and histone methylation. Nature *585*, 277–282. https://doi.org/10.1038/s41586-020-2682-1.

41. Panisova, E., Kery, M., Sedlakova, O., Brisson, L., Debreova, M., Sboarina, M., Sonveaux, P., Pastorekova, S., and Svastova, E. (2017). Lactate stimulates CA IX expression in normoxic cancer cells. Oncotarget *8*, 77819–77835. https://doi.org/10.18632/oncotarget.20836.

42. Goetze, K., Walenta, S., Ksiazkiewicz, M., Kunz-Schughart, L.A., and Mueller-Klieser, W. (2011). Lactate enhances motility of tumor cells and inhibits monocyte migration and cytokine release. Int. J. Oncol. *39*, 453–463. https://doi.org/10.3892/ijo.2011.1055.

43. Zong, Z., Xie, F., Wang, S., Wu, X., Zhang, Z., Yang, B., and Zhou, F. (2024). Alanyl-tRNA synthetase, AARS1, is a lactate sensor and lactyltransferase that lactylates p53 and contributes to tumorigenesis. Cell *187*, 2375–2392.e33. https://doi.org/10.1016/j.cell.2024.04.002.

44. Chen, H., Li, Y., Li, H., Chen, X., Fu, H., Mao, D., Chen, W., Lan, L., Wang, C., Hu, K., et al. (2024). NBS1 lactylation is required for efficient DNA repair and chemotherapy resistance. Nature *631*, 663–669. https://doi.org/10.1038/s41586-024-07620-9.

45. Végran, F., Boidot, R., Michiels, C., Sonveaux, P., and Feron, O. (2011). Lactate influx through the endothelial cell monocarboxylate transporter MCT1 supports an NF-κB/IL-8 pathway that drives tumor angiogenesis. Cancer Res. *71*, 2550–2560. https://doi.org/10.1158/0008-5472.Can-10-2828.

46. Shi, S., Xu, J., Zhang, B., Ji, S., Xu, W., Liu, J., Jin, K., Liang, D., Liang, C., Liu, L., et al. (2016). VEGF Promotes Glycolysis in Pancreatic Cancer via HIF1α Up-Regulation. Curr. Mol. Med. *16*, 394–403. https://doi.org/10.2174/1566524016666160316153623.

47. Brand, A., Singer, K., Koehl, G.E., Kolitzus, M., Schoenhammer, G., Thiel, A., Matos, C., Bruss, C., Klobuch, S., Peter, K., et al. (2016). LDHA-Associated Lactic Acid Production Blunts Tumor Immunosurveillance by T and NK Cells. Cell Metab. *24*, 657–671. https://doi.org/10.1016/j.cmet.2016.08.011.

48. Reinfeld, B.I., Madden, M.Z., Wolf, M.M., Chytil, A., Bader, J.E., Patterson, A.R., Sugiura, A., Cohen, A.S., Ali, A., Do, B.T., et al. (2021). Cell-programmed nutrient partitioning in the tumour microenvironment. Nature *593*, 282–288. https://doi.org/10.1038/s41586-021-03442-1.

49. Yu, L., Liebenberg, K., Shen, Y., Liu, F., Xu, Z., Hao, X., Wu, L., Zhang, W., Chan, H.L., Wei, B., et al. (2025). Tumor-derived arachidonic acid reprograms neutrophils to promote immune suppression and therapy resistance in triple-negative breast cancer. Immunity *58*, 909–925.e7. https://doi.org/10.1016/j.immuni.2025.03.002.

50. Zhu, Y., Zhou, Z., Du, X., Lin, X., Liang, Z.M., Chen, S., Sun, Y., Wang, Y., Na, Z., Wu, Z., et al. (2025). Cancer cell-derived arginine fuels polyamine biosynthesis in tumor-associated macrophages to promote immune evasion. Cancer Cell *43*, 1045–1060.e7. https://doi.org/10.1016/j.ccell.2025.03.015.

51. Xiao, Y.肖., Xu, Y.徐., Wang, H.王., Yang, F.杨., Ding, X.H.丁., Fu, T.傅., Chen, L.陈., Jin, X.金., Zhao, Y.X.赵., Wang, Y.王., et al. (2025). HEBP2-governed glutamine competition between tumor and macrophages dictates immunotherapy efficacy in triple-negative breast cancer. Cell Metab. *37*, 2030–2047.e7. https://doi.org/10.1016/j.cmet.2025.08.009.

52. Noble, R.A., Thomas, H., Zhao, Y., Herendi, L., Howarth, R., Dragoni, I., Keun, H.C., Vellano, C.P., Marszalek, J.R., and Wedge, S.R. (2022). Simultaneous targeting of glycolysis and oxidative phosphorylation as a therapeutic strategy to treat diffuse large B-cell lymphoma. Br. J. Cancer *127*, 937–947. https://doi.org/10.1038/s41416-022-01848-w.

53. Silva, A., Félix, A., Cerqueira, M., Gonçalves, C.S., Sampaio-Marques, B., Longatto-Filho, A., Baltazar, F., and Afonso, J. (2023). Effects of Lactate Transport Inhibition by AZD3965 in Muscle-Invasive Urothelial

Bladder Cancer. Pharmaceutics *15*, 2688. https://doi.org/10.3390/pharmaceutics15122688.

54. Kumagai, S., Koyama, S., Itahashi, K., Tanegashima, T., Lin, Y.T., Togashi, Y., Kamada, T., Irie, T., Okumura, G., Kono, H., et al. (2022). Lactic acid promotes PD-1 expression in regulatory T cells in highly glycolytic tumor microenvironments. Cancer Cell *40*, 201–218.e9. https://doi.org/10.1016/j.ccell.2022.01.001.

55. Niveau, C., Cettour-Cave, M., Mouret, S., Sosa Cuevas, E., Pezet, M., Roubinet, B., Gil, H., De Fraipont, F., Landemarre, L., Charles, J., et al. (2025). MCT1 lactate transporter blockade re-invigorates anti-tumor immunity through metabolic rewiring of dendritic cells in melanoma. Nat. Commun. *16*, 1083. https://doi.org/10.1038/s41467-025-56392-x.

56. Lopez, E., Karattil, R., Nannini, F., Weng-Kit Cheung, G., Denzler, L., Galvez-Cancino, F., Quezada, S., and Pule, M.A. (2023). Inhibition of lactate transport by MCT-1 blockade improves chimeric antigen receptor T-cell therapy against B-cell malignancies. J. Immunother. Cancer *11*, e006287. https://doi.org/10.1136/jitc-2022-006287.

57. Fang, Y., Liu, W., Tang, Z., Ji, X., Zhou, Y., Song, S., Tian, M., Tao, C., Huang, R., Zhu, G., et al. (2023). Monocarboxylate transporter 4 inhibition potentiates hepatocellular carcinoma immunotherapy through enhancing T cell infiltration and immune attack. Hepatology *77*, 109–123. https://doi.org/10.1002/hep.32348.

58. Rainone, P., Valtorta, S., Villa, C., Todde, S., Cadamuro, M., Bertoli, G., Conconi, D., Lavitrano, M., and Moresco, R.M. (2023). Evaluating [(18)F]FDG and [(18)F]FLT Radiotracers as Biomarkers of Response for Combined Therapy Outcome in Triple-Negative and Estrogen-Receptor-Positive Breast Cancer Models. Int. J. Mol. Sci. *24*, 14124. https://doi.org/10.3390/ijms241814124.

59. Toyoda, K., Yasunaga, J.I., Shichijo, T., Arima, Y., Tsujita, K., Tanaka, A., Salah, T., Zhang, W., Hussein, O., Sonoda, M., et al. (2023). HTLV-1 bZIP Factor-Induced Reprogramming of Lactate Metabolism and Epigenetic Status Promote Leukemic Cell Expansion. Blood Cancer Discov. *4*, 374–393. https://doi.org/10.1158/2643-3230.Bcd-22-0139.

60. Yu, T., Liu, Z., Tao, Q., Xu, X., Li, X., Li, Y., Chen, M., Liu, R., Chen, D., Wu, M., and Yu, J. (2024). Targeting tumor-intrinsic SLC16A3 to enhance anti-PD-1 efficacy via tumor immune microenvironment reprogramming. Cancer Lett. *589*, 216824. https://doi.org/10.1016/j.canlet.2024.216824.

61. Heinrich, T., Sala-Hojman, A., Ferretti, R., Petersson, C., Minguzzi, S., Gondela, A., Ramaswamy, S., Bartosik, A., Czauderna, F., Crowley, L., et al. (2021). Discovery of 5-{2-[5-Chloro-2-(5-ethoxyquinoline-8-sulfonamido)phenyl]ethynyl}-4-methoxypyridine-2-carboxylic Acid, a Highly Selective in Vivo Useable Chemical Probe to Dissect MCT4 Biology. J. Med. Chem. *64*, 11904–11933. https://doi.org/10.1021/acs.jmedchem.1c00448.

62. Kawatkar, A., Clark, R.A., Hopcroft, L., Roaquin, D.A., Tomlinson, R., Zuhl, A.M., Lamont, G.M., Kettle, J.G., Critchlow, S.E., Castaldi, M.P., et al. (2023). Chemical Biology Approaches Confirm MCT4 as the Therapeutic Target of a Cellular Optimized Hit. ACS Chem. Biol. *18*, 296–303. https://doi.org/10.1021/acschembio.2c00666.

63. Goldberg, F.W., Kettle, J.G., Lamont, G.M., Buttar, D., Ting, A.K.T., McGuire, T.M., Cook, C.R., Beattie, D., Morentin Gutierrez, P., Kavanagh, S.L., et al. (2023). Discovery of Clinical Candidate AZD0095, a Selective Inhibitor of Monocarboxylate Transporter 4 (MCT4) for Oncology. J. Med. Chem. *66*, 384–397. https://doi.org/10.1021/acs.jmedchem.2c01342.

64. Zhou, D.D., Bai, W.Q., Zhai, X.T., Sun, L.P., Zhen, Y.S., Li, Z.R., and Miao, Q.F. (2021). Excellent effects and possible mechanisms of action of a new antibody-drug conjugate against EGFR-positive triple-negative breast cancer. Mil. Med. Res. *8*, 63. https://doi.org/10.1186/s40779-021-00358-9.

65. Spring, L.M., Tolaney, S.M., Fell, G., Bossuyt, V., Abelman, R.O., Wu, B., Maheswaran, S., Trippa, L., Comander, A., Mulvey, T., et al. (2024). Response-guided neoadjuvant sacituzumab govitecan for localized triple-negative breast cancer: results from the NeoSTAR trial. Ann. Oncol. *35*, 293–301. https://doi.org/10.1016/j.annonc.2023.11.018.

66. Bardia, A., Rugo, H.S., Tolaney, S.M., Loirat, D., Punie, K., Oliveira, M., Brufsky, A., Kalinsky, K., Cortés, J., Shaughnessy, J.O., et al. (2024). Final Results From the Randomized Phase III ASCENT Clinical Trial in Metastatic Triple-Negative Breast Cancer and Association of Outcomes by Human Epidermal Growth Factor Receptor 2 and Trophoblast Cell Surface Antigen 2 Expression. J. Clin. Oncol. *42*, 1738–1744. https://doi.org/10.1200/jco.23.01409.

67. Coates, J.T., Sun, S., Leshchiner, I., Thimmiah, N., Martin, E.E., McLoughlin, D., Danysh, B.P., Slowik, K., Jacobs, R.A., Rhrissorrakrai, K., et al. (2021). Parallel Genomic Alterations of Antigen and Payload Targets Mediate Polyclonal Acquired Clinical Resistance to Sacituzumab Govitecan in Triple-Negative Breast Cancer. Cancer Discov. *11*, 2436–2445. https://doi.org/10.1158/2159-8290.CD-21-0702.

68. Cortes, J., Rugo, H.S., Cescon, D.W., Im, S.A., Yusof, M.M., Gallardo, C., Lipatov, O., Barrios, C.H., Perez-Garcia, J., Iwata, H., et al. (2022). Pembrolizumab plus Chemotherapy in Advanced Triple-Negative Breast Cancer. N. Engl. J. Med. *387*, 217–226. https://doi.org/10.1056/NEJMoa2202809.

69. Schmid, P., Cortes, J., Dent, R., McArthur, H., Pusztai, L., Kümmel, S., Denkert, C., Park, Y.H., Hui, R., Harbeck, N., et al. (2024). Overall Survival with Pembrolizumab in Early-Stage Triple-Negative Breast Cancer. N. Engl. J. Med. *391*, 1981–1991. https://doi.org/10.1056/NEJMoa2409932.

70. Hegde, P.S., and Chen, D.S. (2020). Top 10 Challenges in Cancer Immunotherapy. Immunity *52*, 17–35. https://doi.org/10.1016/j.immuni.2019.12.011.

STAR★METHODS

KEY RESOURCES TABLE

REAGENT or RESOURCE	SOURCE	IDENTIFIER
Antibodies		
IHC: anti-CD45	Abcam	Cat# Ab10558; RRID: AB_442810
IHC: anti-CD11b	Abcam	Cat# Ab133357; RRID: AB_2650514
IHC: anti-MPO	Proteintech	Cat# 66177-1-Ig; RRID: AB_2881572
IHC: anti-MCT1	Proteintech	Cat# 20139-1-AP; RRID: AB_2878645
IHC: anti-MCT4	Proteintech	Cat# 22787-1-AP; RRID: AB_11182479
IHC: anti-GLUT3	Proteintech	Cat# 20403-1-AP; RRID: AB_10694437
FC: anti-mouse CD16/32 (clone 93)	BioLegend	Cat# 101320; RRID: AB_1574975
FC: Zombie-RED	BioLegend	Cat# 423110
FC: APC/FIRE 750 anti-mouse CD45 (clone I3/2.3)	BioLegend	Cat# 147714; RRID: AB_2750441
FC: PerCP/Cyanine5.5 anti-mouse CD3e (clone 145-2C11)	BioLegend	Cat# 100328; RRID: AB_893318
FC: Alexa Fluor 700 anti-mouse CD4 (clone RM4-5)	BioLegend	Cat# 100536; RRID: AB_493701
FC: FITC anti-mouse CD8a (clone 53–6.7)	BioLegend	Cat# 100706; RRID: AB_312745
FC: PE anti-human/mouse GZMB (clone QA16A02)	BioLegend	Cat# 372208; RRID: AB_2687032
FC: APC anti-mouse PRF (clone S16009B)	BioLegend	Cat# 154404; RRID: AB_2721465
FC: APC anti-mouse IFN-gamma (clone XMG1.2)	BioLegend	Cat# 505809; RRID: AB_315403
FC: PE anti-mouse PD-1 (clone 29F.1A12)	BioLegend	Cat# 135205; RRID: AB_1877232
FC: FITC anti-mouse/human CD11b (clone M1/70)	BioLegend	Cat# 101206; RRID: AB_312789
FC: PerCP/Cyanine5.5 anti-mouse F4/80 (clone BM8)	BioLegend	Cat# 123127; RRID: AB_893496
FC:PE anti-mouse CD86 (clone GL-1)	BioLegend	Cat# 105006; RRID: AB_313149
FC: APC anti-mouse CD206 (clone C068C2)	BioLegend	Cat# 141707; RRID: AB_10896057
InVivoMab anti-mouse PD-1 (clone RMP1-14)	BioXcell	Cat# BE0146; RRID: AB_10949053
InVivoMab rat IgG2a isotype control (clone : 2A3)	BioXcell	Cat# BP0089; RRID: AB_1107769
Biological samples		
TNBC tumor samples	This study	FUSCCTNBC
FFPE sections from patients in the FUSCC cohort	This study	N/A
Chemicals, peptides, and recombinant proteins		
Polybrene	Sigma Aldrich	Cat# H9268
Puromycin	Sangon Biotech	Cat# A610593-0025
Recombinant Murine M-CSF	PeproTech	Cat# 315-02
Recombinant Human M-CSF	PeproTech	Cat# 300-25
Critical commercial assays		
ChamQ Universal SYBR qPCR Master Mix	Vazyme	Cat# Q711-02
HiScript III All-in-one RT SuperMix Perfect for qPCR	Vazyme	Cat# R333-01
MycoBlueTM Mycoplasma Detector	Vazyme	Cat# D101-01
Lipofectamine RNA iMAX	Invitrogen	Cat# 13778150
Dispase II	Roche	Cat# 04942078001
Hyaluronidase	Sigma	Cat# H3506
Collagenase	Sigma	Cat# C0130
Cell Activation Cocktail (with Brefeldin A)	BioLegend	Cat# 423304
RBC Lysis Buffer (10x)	BioLegend	Cat# 420302
Intracellular Staining Permeabilization Wash Buffer (10x)	BioLegend	Cat# 421002

(*Continued on next page*)

Continued

REAGENT or RESOURCE	SOURCE	IDENTIFIER
Fixation Buffer	BioLegend	Cat# 420801
Cyto-Last™ Buffer	BioLegend	Cat# 422501
Cell Staining Buffer	BioLegend	Cat# 420201
Opal Polaris 7-Color Manual IHC Kit	AKOYA Biosciences	Cat# NEL861001KT
Cell Counting Kit-8	Yeasen	Cat# 40203ES92
BCA protein assay reagent	Solarbio	Cat# PC0020
TRIzol reagent	Invitrogen	Cat# 15596018CN
Sacituzumab govitecan	Trodelvy	–
Deposited data		
FUSCCTNBC scRNA-seq	This study	The National Omics Data Encyclopedia, OEP003394
BioKey	(Bassez et al., 2021)	https://ega-archive.org/EGAS00001004809
4T1 orthotopic tumor scRNA-seq	(Sebastian et al., 2020)	https://datadryad.org
Experimental models: Cell lines		
Human breast cancer cell HCC1806	ATCC	Cat# CRL-2335; RRID: CVCL_1258
Human breast cancer cell Hs578T	ATCC	Cat# CRL-7849; RRID: CVCL_0332
Human breast cancer cell BT549	ATCC	Cat# HTB-122; RRID: CVCL_1092
Human breast cancer cell MDA-MB-231	ATCC	Cat# HTB-26; RRID: CVCL_0062
Human monocytic cell line THP-1	ATCC	Cat# TIB-202; RRID: CVCL_A4CA
Mouse macrophage cell line Raw264.7	ATCC	Cat# TIB-71; RRID: CVCL_0493
Mouse breast cancer cell 4T1	Y. Kang Lab	N/A
Mouse breast cancer cell AT3	Y. Kang Lab	N/A
Human embryonic kidney cell HEK293T	ATCC	Cat# CRL-3216; RRID: CVCL_0063
Experimental models: Organisms/strains		
Mouse strain: C57BL/6	Shanghai Jihui Laboratory Animal Care	N/A
Mouse strain: BALB/c	Shanghai Jihui Laboratory Animal Care	N/A
Mouse strain: Nude	Shanghai Jihui Laboratory Animal Care	N/A
Mouse strain: NOD-Prkdc^{scid}Il2rg^{null}	Shanghai Jihui Laboratory Animal Care	N/A
Software and algorithms		
R 4.2.1	R Core Team	https://www.r-project.org/
Seurat	(Hao et al., 2021)	https://satijalab.org/seurat/
Compass	Prof. Nir Yosef's lab Github page	https://github.com/YosefLab/Compass
ImageJ	NIH	https://imagej.nih.gov/ij/
Graphpad Prism 9.0.0	GraphPad Software	http://www.graphpad.com/
Flowjo	FlowJo, LLC	https://www.flowjo.com/
CytExpert	Beckman Coulter	www.beckmancoulter.com
Biorender	N/A	https://biorender.com/
Cell Ranger	10× Genomics	https://www.10xgenomics.com/support/software/cell-ranger/latest
Vectra Polaris	AkoyaBio	http://www.akoyabio.com
Phenochart	AkoyaBio	http://www.akoyabio.com

EXPERIMENTAL MODEL AND STUDY PARTICIPANT DETAILS

Patients and clinical samples

Our study included 27 female patients with histologically confirmed TNBC receiving neoadjuvant therapy in Fudan University Shanghai Cancer Center (FUSCC) (clinical information was detailed in Table S1). Among these, eighteen patients received the combination of chemotherapy and anti-PD-1, while seven patients received chemotherapy alone. The rest two patients were included, one was lost during follow-up, and treatment information for the other was unavailable. Prior to the initiation of treatment, tumor biopsies were collected from all participants and subjected to scRNA-seq.

All tissue samples included in this study were obtained after approval of the research by the FUSCC Ethics Committee. Information on race, ethnicity, and ancestry was not collected in this study.

Human and mouse TNBC cell lines

The human breast cancer cell lines MDA-MB-231, Hs 578T, BT-549, human monocytic cell line THP-1, human embryonic kidney cell line HEK293T, and mouse macrophage cell line Raw264.7 were obtained from American Type Culture Collection (ATCC). The murine TNBC cell lines, 4T1 and AT3 were obtained from Y. Kang's laboratory (Princeton University, USA). All the cell lines were authenticated by monitoring cell vitality, mycoplasma contamination, and short tandem repeat profiling. Immediately upon receipt, the cells were expanded and frozen into numerous aliquots. HEK293T cells were employed for lentiviral packaging to produce MCT1-or MCT4-knockdown stable lines. All functional experiments presented in this study were performed in well-established human and murine TNBC cell lines. All cell lines were cultured in complete growth medium as previously described. Only cells within 6 months from being thawed were used for the current study.

Murine models

Five-to six-week-old female BALB/c and nude mice were obtained from Shanghai Jihui Laboratory Animal Care. Mice were housed under 12 h light/dark cycles and ambient temperature (20°C–22°C) and humidity (60 ± 10%), with free access to standard rodent diet and water in individually ventilated cages in a specific pathogen free facility monitoring health status with culture, serum and microscopic examination.

Human and mouse myeloid cells preparation

Peripheral blood from healthy donors was acquired from Fudan University Shanghai Cancer Center, after all the written informed consent were provided. Mononuclear cells were isolated by Ficoll density gradient centrifugation, plated in 6-well plates, and cultured in complete RPMI 1640 medium supplemented with 10ng/mL macrophages colony-stimulating factor (M-CSF). Medium was changed every 2 days, and differentiated myeloid cells were used for experiments on day 7.

Mouse myeloid cells were isolated from the bone marrow of 6- to 8-week-old female C57BL/6 mice or BALB/c mice. Briefly, bone marrow was flushed out, cultured, and differentiated in complete RPMI 1640 medium supplemented with 10 ng/mL M-CSF for 7 days.

In vivo mouse studies

All animal experiments were performed according to protocols approved by the Research Ethical Committee of Fudan University Shanghai Cancer Center (IACUC Protocols # FUSCC-IACUC-2025679, FUSCC-IACUC-2025678, FUSCC-IACUC-2025101, FUSCC-IACUC-2024232 and FUSCC-IACUC-2024457). 4T1, AT3, or MDA-MB-231 TNBC cells were injected subcutaneously into the mammary fat pad region of the mice. For the immunotherapy combination therapy assay, after the tumor volume reached the specific size, the mice were divided into 4 groups: 1) treated with DMSO and IgG; 2) treated with DMSO plus anti-PD-1; 3) treated with MCT1 inhibitor plus isotype IgG; 4) treated with MCT1 inhibitor plus anti-PD-1. For the SG combination therapy assay, the mice were randomly divided into 4 groups: 1) treated with DMSO; 2) treated with MCT1 inhibitor; 3) treated with SG; 4) treated with MCT1 inhibitor plus SG. Tumor size was measured every three days using a caliper. Tumor volume in mm^3 was calculated using the following formula: tumor volume = $0.5 \times L \times W^2$, where L is the longest dimension and W is the perpendicular dimension. For the PDX model, tumors from PDX-bearing NOD-$Prkdc^{scid}$ $Il2rg^{null}$ (NPSG) mice were cut into pieces and subcutaneously implanted into the flanks of NPSG mice (6-week-old females). Treatment was started when tumors grew to a specified size, and mice were randomly assigned to the same 4 groups.

METHOD DETAILS

scRNA-seq data pre-processing and quality control

Raw fastq files were firstly processed by the Cell Ranger software pipeline (version 3.1.0, 10× Genomics) to demultiplex cellular barcodes and map reads to GRCh38 reference genome (Genome Reference Consortium Human Build 38) to generate matrices of gene counts by cell barcodes. We used Seurat package (version 4.3.0) in R (version 4.2.1) to process the unique molecular identifier (UMI) count matrix and conduct downstream analysis. For quality controls, we applied the criteria to filter out cells with UMI/gene numbers less than 200 or more than 8000, percentage of mitochondrial counts <20%, and percentage of ribosome counts <20%.

Visualization and clustering

Cells with low gene counts, high mitochondrial gene percentages, or potential doublets were excluded. For the downstream analysis, we employed the R package Harmony, to integrate the data and correct the batch effect derived from patient-specific expression patterns. Then, the batch-corrected matrix was input into Seurat and perform standard Seurat workflow. The top 2,000 highly variable genes were selected, and dimensionality reduction was performed by PCA. The top 30 principal components were chosen based on the ElbowPlot and used for kNN-based clustering at a resolution of 0.8. Cell clusters were visualized using UMAP.

Cell type annotation

We annotated cell types based on the expression of known marker genes as described previously, i.e., CD2, CD3D and CD3E for T cell; COL1A1, DCN, and C1R for fibroblast; LYZ, CD68 and TYROBP for myeloid cell; CD24, KRT19, and SCGB2A2 for cancer cell; CD79A, MZB1, and MS4A1 for B cell; CLDN5, FLT1, and RAMP2 for endothelial cell (Figure 1D).

Metabolic gene sets construction

We integrated metabolic genes and metabolic pathways from five distinct data resources, including Kyoto Encyclopedia of Genes and Genomes (KEGG), Recon3D, Human-GEM, Reactome, and BRENDA. All metabolic genes are listed in Table S2 and included in the metabolic heterogeneity analysis in Figure 2.

Differentially expressed metabolic genes analysis

Differentially expressed genes (DEGs) were identified using the MAST test with *FindMarkers* and *FindAllMarkers* functions in Seurat without a threshold for logFC and for expression in a minimum fraction of cells. Among these, metabolic genes were extracted for further analysis.

Calculation of metabolic pathway activities

We applied two different methods to calculate the metabolic pathway activities:

(1) Gene set enrichment analysis (GSEA) was performed to evaluate and visualize the enrichment of metabolic pathways across different cell types. The analysis was conducted using the clusterProfiler R package with default parameters, and the normalized enrichment scores (NES) were used to represent pathway activity.
(2) scMetabolism: an R package, which integrates dropout gene imputation, metabolism quantification, and data visualization.

Compass analysis

Compass algorithm was employed to characterize cellular metabolic fluxes at single-cell resolution. Briefly, using the Recon2 metabolic network as reference and constraint-based models as main principle, Compass quantifies the potential activity of each metabolic reaction for the downstream analysis as the single-cell level. We defined the core metabolic reactions as described and computed the Compass scores following the default parameters. To compare the differential potential-activity of reactions according to the Compass predictions, we computed for each reaction by the Wilcoxon's rank sum between the Compass scores in the two different cell types. Effect size was then evaluated with Cohen's d statistic, defined as the difference between the sample means over the pooled sample standard deviation.

The resulting p values are adjusted using Benjamini-Hochberg (BH) method. If the adjusted p value is smaller than 0.1, we supposed the reaction is differentially active.

Single-cell metabolic features-treatment interaction analysis

To quantify metabolic activity at single-cell resolution, metabolic pathway scores were computed for each major cell type in every patient. For downstream association analyses, each metabolic feature (pathway score or gene expression) was summarized at the patient level. Logistic regression models were applied to assess whether these metabolic features were associated with treatment response, modeled as: Efficacy (pCR vs. non-pCR) $\sim$ Biomarker. Models were fitted using the glm function with a binomial family, and significance was evaluated using Wald test–derived p values.

Multiplex immunofluorescence staining

The formalin-fixed paraffin-embedded (FFPE) tissue microarray containing human TNBC was acquired from Fudan University Shanghai Cancer Center. The slides were processed using the Opal Polaris 7-Color Manual IHC Kit according to the manufacturer's protocol. In brief, FFPE sections were dewaxed, and epitope retrieval was performed. After blocking, the slides were incubated with primary antibodies followed by signal amplification of opal fluorophores and antibody stripping. The slides were then counterstained with spectral DAPI. The primary antibodies were anti-MPO (Proteintech, 1:500), anti-CD11b (Abcam, 1:4000), anti-GLUT3 (Proteintech, 1:1000), anti-MCT1 (Proteintech, 1:500), and anti-MCT4 (Proteintech, 1:1000). Images were then serially acquired for each channel and thresholds were set for each channel to assign positivity using Vectra Polaris software. These data are then used to quantify cellular phenotypes of interest using Phenochart software.

Immunohistochemical staining

Immunohistochemical staining of primary tumors were performed by Wuhan Servicebio Technology with the following antibodies overnight: anti-CD45, anti-CD11b, anti-MCT1, anti-MCT4, anti-GLUT3, and stained with goat anti-rat IgG Ab at room temperature and counterstained with hematoxylin.

Stable isotope labeling (SIL) and metabolomics

For stable isotope labeling, media was switched to in glucose- and glutamine-free RPMI supplemented with 10% FBS, 1% Penicillin/Streptomycin, 50mM β-mercaptoethanol, 1% HEPES, 1× non-essential amino acids, containing 10mM U-13C-glucose, or 20mM U-13C-L-Lactate for 6 h. The intracellular and medium metabolites were extracted according to the manufacturer's protocol.

RNA isolation and quantitative real-time PCR (qRT-PCR)

Total RNA was isolated using TRIzol reagent (Invitrogen, #15596018CN) and then transcribed into cDNA using HiScript III All-in-one RT SuperMix Perfect for qPCR (Vazyme, #R333-01) according to the manufacturer's protocol. qPCR was performed using ChamQ Universal SYBR qPCR Master Mix (Vazyme, #Q711-02). The housekeeping gene GAPDH was used as internal control.

Transfection of small interfering RNAs

Small interfering RNAs (siRNA) were transfected into myeloid cells and TNBC cells using Lipofectamine RNAiMAX. SiRNAs specific for GLUT3, MCT1 and MCT4 were purchased from Guangzhou RiboBio Co., Ltd, while a scrambled non-targeting siRNA was used as negative control. Briefly, the RNAi duplex-Lipofectamine RNAiMAX complexes were prepared according to the manufacturer's protocol, with a final volume of 600 μL and a final RNA concentration of 10 nM. Then we added the mix to each well containing cells, and incubated the cells 72 h to ensure the efficiency of knockdown.

In vitro cell viability assays

For short-term cell viability assays, cells were plated using optimal seeding densities per well in 96-well plates with their corresponding growth medium and allowed to adhere overnight. The day after the cells reached 75–80% confluence, the medium was refreshed or replaced by the conditioned medium as described. After the co-culture induction or the enough confluence, cell viability was assessed by Cell Counting Kit-8 (Yeasen, #40203ES92). The absorbance was measured at 450 nm (A450).

In vitro cell migration and invasion assays

For the cell migration and invasion assays, cells were suspended in serum-free medium and plated using optimal seeding densities in the top chambers. The top chambers were coated with Matrigel (Corning) for the invasion assay; while the migration assay did not include this step. The lower chambers contained 600 μL of medium supplemented with 10% FBS. After incubation for 4–16 h, the cells on the underside of the filter membrane were fixed with methanol for 20 min. The unmigrated and uninvaded cells were removed using cotton swabs, and the cells that had migrated or invaded through the filter membrane were then stained with 0.1% crystal violet, photographed, and counted using ImageJ.

Flow cytometry analysis

For flow cytometry analysis after *in vivo* experiments, mouse tumors were mechanically dissociated with scissors and digested with 20 mg/mL dispase II, 20 mg/mL collagenase I and 20 mg/mL hyaluronidase for 30–60 min at 37°C with rotation. Cell suspensions were then filtered through 100-μm and 40-μm cell strainers and resuspended in PBS. Red blood cells were lysed with red blood cell lysis buffer for 10 min on ice. Cells were then washed in PBS and stained with Zombie-Red viability assay at a 1/1000 dilution. for 20 min at 4°C. A monoclonal antibody to CD16/32 was used to block cells before staining with antibody panels. Then, the single-cell suspensions were washed in Cell Staining Buffer and incubated with the indicated flow antibodies at 4°C for 30 min. All the antibodies and reagents used for flow cytometry included CD45, CD3e, CD4, CD8, GZMB, PRF, PD1, IFN-gamma, CD11b, F4/80, CD86, and CD206. For intracellular staining, cells were stimulated with Leukocyte Activation Cocktail for 6 h and then fixed and permeabilized by using Fixation Buffer and Intracellular Staining Permeabilization Wash Buffer according to the manufacturers' instructions. Permeabilized cells were then incubated with fluorescently labeled antibodies against GZMB and PRF1 for 30 min at 4°C. A CytoFLEX S flow cytometer (Beckman Coulter) and FlowJo software (Version 10.5.3, TreeStar) were used for further analyses.

QUANTIFICATION AND STATISTICAL ANALYSIS

Statistical analyses were performed using Prism (version 9.0.0) or R (version 4.2.1). Statistical significance was determined using the unpaired Student's *t* test, Mann-Whitney test, one-way ANOVA test, or Kruskal-Wallis test when appropriate. All data were presented as the mean ± SEM of at least three independent experiments unless otherwise indicated in the figure legend. All cell-based *in vitro* experiments were independently repeated three times in triplicate. Unless otherwise specified, two-sided *p* values less than 0.05 were statistically significant. *p*-values and sample size can be found in main and supplementary figure legends.